J. Fluid Mech. (2019), *vol.* 880, *pp.* 1036–1069.
doi:10.1017/jfm.2019.739

Experimental investigation of the wave-induced motion of and force distribution along a flexible stem

Niels G. Jacobsen[1,†], Wout Bakker[2,3], Wim S. J. Uijttewaal[4] and Rob Uittenbogaard[2]

[1]Harbour, Coastal and Offshore, Deltares, 2629HV Delft, The Netherlands

[2]Numerical Simulation Software, Deltares, 2629HV Delft, The Netherlands

[3]EcoFlows, 1015BL Amsterdam, The Netherlands

[4]Environmental Fluid Mechanics, Hydraulic Engineering, Delft University of Technology, 2628CN Delft, The Netherlands

(Received 12 October 2018; revised 26 July 2019; accepted 3 September 2019; first published online 18 October 2019)

The work presents an experimental investigation into the motion of and hydrodynamic forces along a single flexible stem in regular waves. The experiment covers a large range in relevant non-dimensional parameters: the drag-to-stiffness ratio $CaL \in [0.003, 3.8]$, the inertia-to-stiffness ratio $CaL/KC \in [4 \times 10^{-5}, 14.8]$, the Keulegan–Carpenter number $KC \in [3.8, 145]$ and the Reynolds number $Re \in [230, 2900]$. The two first parameters relate to the response of the stem in waves and thus account for material properties, while the two last parameters are relevant for hydrodynamic forces on the stem. The displacement of the stem was captured with a digital video camera and the displacement along the stem was captured for every 2.5 mm at 25 Hz. This unique laboratory data set allowed for the following analyses: (i) Determination of the relevant non-dimensional parameter to predict the stem motion and shape. (ii) A direct comparison between the measured force for mimics of two lengths (0.15 m and 0.30 m) illustrating the force reduction potential for flexible mimics. (iii) Direct evaluation of the average force coefficients C_D (drag) and C_M (inertia) for the flexible stems. (iv) The distributed external hydrodynamic loading and the internal shear forces were estimated from the laboratory experiments. The distribution of the shear force helped to understand the breakage mechanisms of flexible stems. (v) A linkage between phase lags and internal shear forces was suggested. The data set is considered valuable as validation material for numerical models of stem motion in waves.

Key words: coastal engineering, wave–structure interactions

1. Introduction

The understanding of the movement of and forces on submerged, flexible vegetation is of importance in several aspects of coastal engineering. These aspects are for

† Email address for correspondence: niels.jacobsen@deltares.nl

instance the attenuation of waves through a patch of vegetation (Möller *et al.* 2014), wave-induced mean currents (Luhar *et al.* 2010) and the influence of the motion of the vegetation on nutrient uptake (Mullarney & Pilditch 2017) and magnitude and direction of sediment transport (Ros *et al.* 2014; Tinoco & Coco 2018).

The wave attenuation in vegetation fields has been studied extensively in medium scale laboratory experiments (Dubi & Tørum 1994; Anderson & Smith 2014; Maza *et al.* 2015; Losada, Maza & Lara 2016), large scale laboratory experiments (Möller *et al.* 2014) and field campaigns (Vo-Luong & Massel 2008; Bradley & Houser 2009; Jadhav, Chen & Smith 2013; Foster-Martinez *et al.* 2018). A quantification of the wave damping has a direct relevance for the ability to predict wave conditions at the toe of dikes or other coastal structures and, for instance, account for the influence of vegetation on overtopping over dikes (EurOtop 2018; Vuik *et al.* 2018). A common output from wave damping experiments is a bulk drag coefficient related to the amount of dissipation under the assumption of validity of linear wave theory within the canopy. The reported bulk drag coefficients are a function of the velocity attenuation within the canopy (Jadhav *et al.* 2013; Jacobsen, McFall & van der A 2019), so they cannot be used to express the actual force observed by the individual stem.

A spectral dissipation model for vegetation (Suzuki *et al.* 2012) is already included in the spectral wave model SWAN, where the user should define the length, density and bulk drag coefficient of the vegetation. The next improvement of practical engineering models for spectral wave transformation is to include the effect of stem flexibility on the wave damping under varying environmental conditions, e.g. changing length and – possibly – changing drag coefficients with wave climate. Here, the concept of effective length is a feasible approach (Luhar & Nepf 2016; Lei & Nepf 2019). The derivation of the effective length relies on the assumption that the drag coefficient for a flexible stem is the same as the drag coefficient for a corresponding rigid stem under the same hydrodynamic conditions. The length of the rigid stem, which gives the same root force as measured for the flexible stem, is called the effective length. Validity of the assumption of identical drag coefficients has not been found documented in the literature, but a violation of the assumption could explain why some stems have an effective length in excess of unity (e.g. Luhar & Nepf 2016; Lei & Nepf 2019). One of the goals in this work is to derive force coefficients for both flexible and rigid stems.

Ros *et al.* (2014) and Tinoco & Coco (2018) observed experimentally that the presence of vegetation affects the suspended sediment concentration through a change in the turbulent kinetic energy. Furthermore, Zhang & Nepf (2019) saw that generation of wave orbital ripples was suppressed for high stem densities. Once in suspension, the net suspended sediment transport is driven by the mean current, but so far the mean current is mainly described with experiments (Luhar *et al.* 2010; Pujol *et al.* 2013; Abdolahpour, Hambleton & Ghisalberti 2017) and a single numerical study (Chen & Zou 2019). A complete description of the mean current (forcing terms and velocity profile) is still missing in the literature, but it is expected that the gradient in the radiation stress tensor, the near-bed wave streaming stresses, the wave-induced set-up and the mean force on the vegetation all contribute. The listed properties, besides the mean vegetation force, are also relevant for the description of the undertow in the surf zone (Deigaard & Fredsøe 1989; Deigaard, Justesen & Fredsøe 1991; Guannel & Özkan-Haller 2014). Hence, the force on and the force coefficients for the individual stem are of importance for the gradient in the radiation stress tensor following wave damping and both the mean surface gradient and the mean force on the vegetation (Dean & Bender 2006; Wu *et al.* 2011). Consequently,

the mean sediment transport magnitudes will implicitly dependent on the stem motion and the force on the stems.

The discussion above shows that the wave dissipation, the sediment transport and mean flow within a canopy field all depend on the behaviour of the flexible stems and the force distribution along the stem. The lack of experimental evidence of the force coefficients on flexible stems was already discussed. With respect to the description of the stem motion, three different sets of non-dimensional parameters have been identified (Mullarney & Henderson 2010; Luhar & Nepf 2016; Leclercq & De Langre 2018). Leclercq & De Langre (2018) proposed a classification of stem motion in pure oscillatory flow and showed validation for a few cases, but the extension of their classification to real waves is not described. Maza, Lara & Losada (2013), Zeller *et al.* (2014) and Luhar & Nepf (2016) made visual observations of the stem motion in waves, but only the intra-wave tip positions were extracted, so the data are not useful for classification. The three sets of non-dimensional parameters are revisited in this work, where novel experimental data are applied to determine the most suitable non-dimensional parameters.

The present work will address the motion of a single stem under regular waves in a controlled laboratory setting. The motion of the stems is recorded with a digital video camera and the displacement, velocity and acceleration are digitized. This gives a unique set of data to understand the interaction between the wave and stem: displacements, phase lags, relative velocities and the force coefficient as a function of non-dimensional parameters. Finally, the external loading along the stem and the internal shear force are estimated directly from the laboratory experiment. The data set is suitable for the validation of the numerical models for the motion of flexible stems (e.g. Dijkstra & Uittenbogaard 2010; Luhar & Nepf 2016; Leclercq & De Langre 2018). The experimental set-up and procedure are described in § 2. The relevant non-dimensional parameters are discussed in § 3.1, while the remainder of § 3 is devoted to the experimental analysis. A discussion is presented in § 4 and it is followed by conclusions in § 5.

2. Experimental campaign

The experimental investigation was performed in a wave flume at Delft University of Technology (Laboratory of Fluid Mechanics). The flume is 41.5 m long, 0.8 m wide and 0.9 m deep. The purpose of the investigation was to obtain a better understanding of the motion and forcing of a single flexible stem under regular waves. To this end, both point data (surface elevation, velocities and base forces) and video recordings were acquired.

2.1. *Layout and experimental conditions*

The layout of the flume and the placement of the point measurement devices are shown in figure 1. The false bottom in the middle of the flume was required to install the force transducer. A total of seven wave gauges, one force transducer and one EMF (electromagnetic flow meter) were used for point measurements. The EMF was placed at different vertical elevations between 0.025 m to 0.325 m above the bed to reconstruct the velocity profile over the height of the stem. Attention was paid to minimizing wave reflection at the end of the flume by installing a gently sloped porous absorber.

Both the EMF and the wave gauges were developed by Delft Hydraulics. The EMF has a range of 0.0–2.5 m s^{-1} with an accuracy of 0.025 m s^{-1} and the wave gauge

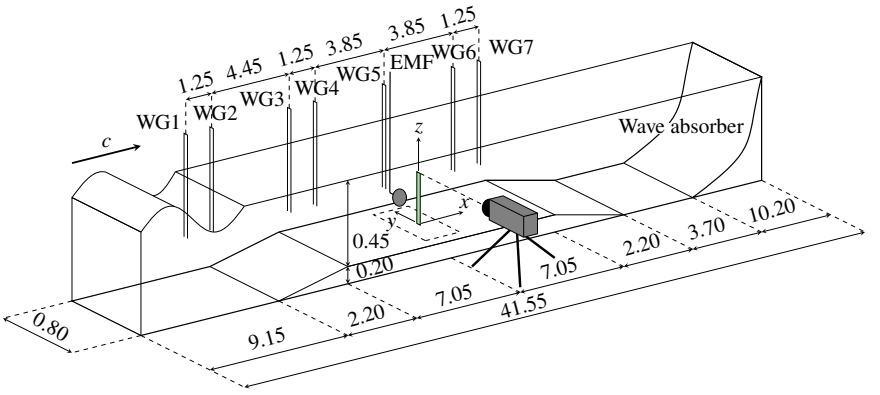

FIGURE 1. (Colour online) Layout of the wave flume with the location of the point instruments. The stem is the green patch in front of the camera. WG, wave gauge. EMF, electromagnetic flow meter.

Name	H (m)	T (s)	N_w (−)	N_s (−)	$\overline{\eta}_t$ (m)	$\overline{\eta}_c$ (m)	$\bar{H}_i$ (m)	$\overline{\varepsilon}_H$ (%)	σ_{ε_H} (%)	$\bar{R}_\eta$ (−)	σ_{R_η} (−)
H040T10	0.04	1.0	59	18	−0.020	0.022	0.042	0.96	0.42	0.9989	0.0003
H040T20	0.04	2.0	73	19	−0.019	0.023	0.041	1.17	0.50	0.9996	0.0008
H070T15	0.07	1.5	63	18	−0.033	0.041	0.074	0.56	0.37	0.9994	0.0002
H070T25	0.07	2.5	67	18	−0.026	0.046	0.072	0.92	0.32	0.9997	0.0006
H110T20	0.11	2.0	75	17	−0.048	0.081	0.129	0.80	0.77	0.9991	0.0005
H110T30	0.11	3.0	77	18	−0.037	0.103	0.141	0.75	0.34	0.9994	0.0006
H160T20	0.16	2.0	73	17	−0.061	0.124	0.185	0.54	1.17	0.9973	0.0031
H160T35	0.16	3.5	79	16	−0.041	0.133	0.175	1.31	0.70	0.9994	0.0004

TABLE 1. Summary of the target wave conditions (columns 1, 2) and the achieved conditions (columns 5, 6, 7). The water depth at the paddle was 0.65 m and 0.45 m at the measuring location. The remaining columns address reproducibility of the wave conditions (see text).

has an accuracy of 1 mm. The plastic mimics were mounted on a force transducer with two screws. The force transducer was from Utilcell (Model 104) and had a range of 1 to 3000 mN and an accuracy of 1 mN. All point measurements were sampled at 100 Hz.

A total of eight wave conditions were studied, see table 1, where H is the regular wave height and T is the wave period. The wave generation was performed with a Bosch Rexroth generator with active reflection compensation and the water depth in front of the paddle was 0.65 m. Each condition was repeated twice, there were four mimics (see below and table 2) and three lengths of the mimic so in total 192 tests were conducted. For each condition, a single stem was mounted on the force transducer and there were no neighbouring stems mimicking a canopy. The duration of the tests varied, but approximately 40 wave periods were generated before the stem motion was recorded. The quantities $\overline{\eta}_c$ and $\overline{\eta}_t$ (table 1) are the average crest and trough elevations, respectively. The average is taken over N_w wave periods (table 1).

Four mimics with rectangular cross-section were used in the experimental campaign to cover a large range of Cauchy numbers (§ 3.1). The mechanical properties and

	Width	Thickness	Young's modulus	Length	Natural period	Density	Material
Symbol	δ_y	δ_x	E	l	T_n	ρ_s	
Name	(mm)	(mm)	(N m^{-2})	(m)	(s)	(kg m^{-3})	
Mimic 1	10.0	0.15	8.7×10^8	{0.15, 0.30}	{4.03, 16.12}	950	Polypropylene
Mimic 2	10.0	0.50	3.3×10^9	{0.15, 0.30}	{0.34, 1.36}	1030	Polystyrene
Mimic 3	8.0	1.60	2.2×10^9	{0.15, 0.30}	{0.07, 0.26}	1090	ABS
Mimic 4	6.0	6.00	2.2×10^9	{0.15, 0.30}	{0.01, 0.03}	1090	ABS

TABLE 2. Mechanical properties of the plastic mimics (E and ρ_s according to manufacturer). The motion of mimic 1 is not treated in this work. The plastic type is given in last column. The natural period, T_n, is described in § 3.1. ABS, acrylonitrile butadiene styrene.

dimensions of the mimics are provided in table 2: δ_y is the width facing the waves, δ_x is the thickness, E is Young's modulus, l is the length and ρ_s the stem density. The force on the mimic was recorded for two values of the length (0.15 m and 0.30 m) and reference tests with no mimic. The tests with no mimic were performed to evaluate whether there were any load recordings from the hydrodynamics on the force transducer itself. This was not the case. Results regarding motion and forces for mimic 2, 3 and 4 are presented in this work, while the motion of mimic 1 is not analysed, because it could not be extracted with the developed tracking software (see appendix B), due to heavy torsion of the stem. The velocities measured for mimic 1 and no mimics are still used in the reconstruction of the velocity profile. The numbering of mimics is retained to allow for consistency with the naming methodology in the underlying data sets.

The adopted coordinate system (x, y, z) has the origin at the base of the stem; x is positive in the wave propagation direction, z is positive upward and y is the horizontal coordinate normal to the wave propagation direction (figure 1).

2.2. *Synchronization*

Synchronization of the data between individual tests is required to reconstruct the velocity field from the N_s number of individual tests. (The value of N_s is reported in table 1 and it is less than 24 for all wave conditions. This comes from the fact some tests were too short to provide a velocity field overlapping the recording video material.) The reconstructed velocity field is needed for the evaluation of relative velocities and force coefficients. The synchronization ensures two aspects: (i) The wave signal is reproducible. (ii) The time axes for all recordings and the video footage are perfectly aligned; see details in appendix A.

The reproducibility is addressed through a zero-crossing analysis yielding individual wave heights H_i of which there are N_w (table 1). The simple average of H_i, $\overline{H}_i$, is reported in table 1 and it is larger than the target at the paddle; an overprediction which can be due to both shoaling over the false bottom and reflection. Similarly, the zero-crossing wave period, T_i, was evaluated and the deviation from target was of the order 10^{-4} s. The reproducibility of the individual wave conditions was evaluated with the error

$$\varepsilon_H(j,k) = \overline{\left(\frac{H_{i,j} - H_{i,k}}{H_{i,j}}\right)}^{i} \quad \text{for } \{j,k\} = 1, \ldots, N_s \tag{2.1}$$

between two tests, with indices j and k for the ith zero-crossing wave. The average and standard deviation over all combinations of j and k are given in table 1 as $\overline{\varepsilon}_H$ and σ_{ε_H}, respectively. The error is 1 % or less, so the reproducibility of the wave conditions is confirmed.

The correlation coefficient between the surface elevation signals for tests j and k was evaluated ($R_\eta(j, k)$) to verify synchronization between tests. The mean ($\overline{R_\eta}$) and standard deviation (σ_{R_η}) of R_η are provided in table 1. These two quantities are, respectively, close to unity and zero, consequently all experiments (for a given wave condition) are confirmed to be aligned in time.

The two velocity components were acquired at the same x-location as the force transducer. The velocity profile was constructed from point measurements of u and w from individual, synchronized tests.

The motion of the stems was captured with a digital video camera (Panasonic DC-HS200) with a sampling frequency of 25 Hz. The local coordinate system was obtained by capturing a gridded frame prior to execution of the tests. The coordinate system had a resolution of approximately 2500 pixel m^{-1} in both horizontal and vertical directions, which equals 0.4 mm pixel^{-1}. The synchronization between the video camera and the point measurements were achieved with a light-emitting diode (LED), see details in § A.3.

3. Results

First, a discussion on relevant non-dimensional parameters is presented. Secondly, the characteristic wave parameters are derived from the measurements. Thirdly, the motion of the stems is described together with the focus on the relative motion between stem and fluid. For instance, the relative velocity is defined as $u_r = u - u_s$ and $w_r = w - w_s$, where the sub-indices r and s mean relative and stem velocities respectively; u and w are the measured flow velocities in the direction of wave propagation (x) and vertical (z) direction and y is the lateral direction.

Once the relative velocity and relative acceleration are evaluated, the average force coefficients for the swaying vegetation are estimated for mimics 2, 3 and 4 (§ 3.4). The average force coefficients are combined with the relative velocities to evaluate the temporal variation of the force along the stem and estimate the internal shear force (§ 3.5).

3.1. *Non-dimensional considerations*

The analysis of non-dimensional quantities is presented based on the Euler–Bernoulli beam theory (small deflections). The unsteady Euler–Bernoulli beam theory with constant EI reads

$$\rho_s \delta_x \delta_y \frac{\partial^2 x_s}{\partial t^2} + EI \frac{\partial^4 x_s}{\partial z^4} = \rho \frac{\delta_y^2}{4} \pi C_M \left(\frac{\partial u}{\partial t} - \frac{\partial^2 x_s}{\partial t^2} \right) + \rho \delta_x \delta_y \frac{\partial u}{\partial t} + \frac{1}{2} \rho C_D \delta_y \left| u - \frac{\partial x_s}{\partial t} \right| \left(u - \frac{\partial x_s}{\partial t} \right). \tag{3.1}$$

The left-hand side describes the acceleration of the stem and the internal elastic forces, where ρ_s is the density of the stem, δ_x and δ_y are cross-sectional dimensions in the x and y directions, x_s is the stem deflection relative to $x = 0$ m in the global coordinate system (figure 1) and t is time; E is Young's modulus and $I = 1/12 \delta_x^3 \delta_y$ is the moment

of inertia. The right-hand side describes the external forcing: the first term is the inertia force; the second term is the Froude–Krylov force and the third term is the drag force. Here, ρ is the density of water, C_M is the inertia coefficient and C_D the drag coefficient.

Equation (3.1) is made non-dimensional with the following choice of non-dimensional parameters: $t_* = t\omega$, $x_* = x/a_w$, $z_* = z/l$ and $u_* = u/u_w$, where $\omega = 2\pi/T$ is the cyclic frequency, u_w a characteristic orbital velocity and $a_w = u_w/\omega$ a characteristic wave orbital excursion. The experimental equivalents to u_w and a_w are defined below. Equation (3.1) becomes

$$\frac{\pi^2}{2} C_M \frac{CaL}{KC}\left(\frac{\partial u_*}{\partial t_*} - \frac{\partial^2 x_{s,*}}{\partial t_*^2}\right) + 2\pi \frac{\delta_x}{\partial_y}\frac{CaL}{KC}\left(\frac{\partial u_*}{\partial t_*} - \frac{\rho_s}{\rho}\frac{\partial^2 x_{s,*}}{\partial t_*^2}\right) \Big/ \frac{\partial^4 x_{s,*}}{\partial z_*^4} + \frac{1}{2} C_D CaL \left|u_* - \frac{\partial x_{s,*}}{\partial t_*}\right| \left(u_* - \frac{\partial x_{s,*}}{\partial t_*}\right), \tag{3.2}$$

where

$$Ca = \frac{\rho \delta_y u_w^2 l^3}{EI}, \quad KC = \frac{2\pi u_w}{\omega \delta_y} \quad \text{and} \quad L = \frac{l}{a_w} = \frac{l\omega}{u_w}. \tag{3.3a–c}$$

Here, Ca is the Cauchy number and describes the ratio of external drag to internal stiffness of the stem, KC is the Keulegan–Carpenter number describing the ratio of drag-to-inertia and L describes the length of the stem to the wave orbital excursion. Mullarney & Henderson (2010), their appendix A, arrived at a similar expression for a circular cross-section, but neglected inertia terms throughout the bulk of their work based on orders of magnitude considerations. Their stiffness parameter, S, is essentially $(CaL)^{-1}$ for a stem with circular cross-section of radius r_0.

Luhar & Nepf (2016) applied $x_* = x/l$ in their analysis of relevant non-dimensional quantities and it led to an involved discussion on dominating quantities, since – for instance – the drag term took the form

$$\frac{1}{2} C_D Ca \left|u_* - L\frac{\partial x_{s,*}}{\partial t_*}\right| \left(u_* - L\frac{\partial x_{s,*}}{\partial t_*}\right). \tag{3.4}$$

They divided the discussion into the regimes $L \ll 1$ and $1 \ll L$ and they stated Ca as the descriptive parameter for $L \ll 1$ and CaL for $1 \ll L$. The two L-regimes follow from their choice in $x_* = x/l$, meaning that the horizontal velocities u and $\partial x_s/\partial t$ were made non-dimensional with two different length scales: l and a_w ($u_w = \omega a_w$). The scaling choices in the present work reduce the total number of combinations of non-dimensional parameters to CaL and CaL/KC. The geometrical ratios δ_x/δ_y and ρ_s/ρ are not considered further in this work.

Leclercq & De Langre (2018) adopted another set of non-dimensional parameters: l as the length scale and $T_n = l^2\sqrt{m_a/EI}$ as the time scale; T_n is the natural period of the submerged stem, where $m_a = \rho\pi\delta_y^2/4$ is the added mass of the submerged stem for a unit added mass coefficient. Leclercq & De Langre (2018) found that the product of the natural period and cyclic wave frequency $T_n\omega = 1$ describes the transition from 'static' regime to their 'convective' and 'modal' regimes for $a_w/l < 1$. They also defined a fourth regime named the 'large-amplitude regime, static reconfiguration with fast reversal' for $1 < a_w/l$. Their classification means that the shape of stem is independent of the magnitude of the oscillatory motion (a_w). In addition to $T_n\omega$, Leclercq & De Langre (2018) found the non-dimensional parameters $L^{-1} = a_w/l$ and

$2/\pi C_D l/\delta_y$. It is easy to realize that $L^{-1} = a_w/l = \delta_y KC/l$. The values of T_n for the present experiment are listed in table 2.

Leclercq & De Langre (2018) studied sinusoidal, oscillatory flow and found that the amplitude of the displacement increased with increasing a_w/l, while the overall shape of the displacement was the same for constant $T_n\omega$. For constant values of a_w/l, the deflection pattern changed from the static regime to more complicated patterns with multiple modes for increasing $T_n\omega$. They did not account for a mean deflection of the stem.

The similarity between the non-dimensional quantities in Leclercq & De Langre (2018), Luhar & Nepf (2016) and the present work is established here. Inserting T_n in the expressions for CaL and CaL/KC gives

$$CaL = 8(T_n\omega)^2 KC = 8(T_n\omega)^2 \frac{a_w}{l}\frac{l}{\delta_y} \tag{3.5}$$

and

$$\frac{CaL}{KC} = \frac{2}{\pi^2}(T_n\omega)^2. \tag{3.6}$$

It is seen that CaL is a product of all three of the non-dimensional quantities suggested by Leclercq & De Langre (2018), while CaL/KC is proportional to the square of $T_n\omega$. The classification by Leclercq & De Langre (2018) is a function of $T_n\omega$ and a_w/l, respectively, therefore it is unlikely that a product of these two parameters (as is the case for CaL) is a suitable non-dimensional parameter. This will be verified in the following.

The transition from the 'static' to 'convective' and 'modal' regimes for $T_n\omega = 1$ corresponds to $CaL/KC = 2/\pi^2 = 0.20$. The value of 0.20 is for an added mass coefficient of 1.0.

3.2. *Characteristic wave parameters*

The characteristic orbital velocity, u_w, and the wave excursion, a_w, are used in the non-dimensional parameters. The following describes how they are calculated from the measured velocities. The characteristic velocity is defined as

$$u_w = \sqrt{2}\langle u_{rms}\rangle_z, \tag{3.7}$$

where u_{rms} is the root-mean-square velocity and $\langle\,\rangle_z$ represents the depth-averaged value over the distance l from the bed. The depth-averaged value is adopted because it represents the dynamics over the full length of the stem better than the velocity at one height in the water column.

The measured velocity signal is decomposed into a mean and a wave part in the following manner:

$$u = \bar{u} + \tilde{u}, \tag{3.8}$$

where $\bar{u}$ is the mean and $\tilde{u}$ the wave component. Normally, a turbulent component is also included in the splitting, but due to the internal filtering of the EMF (7 Hz), the turbulence is assumed filtered out. The splitting in (3.8) is evaluated per vertical level and similarly for the vertical velocity $w = \bar{w} + \tilde{w}$, where $\bar{w} = 0$ m s^{-1}.

The orbital excursion is evaluated directly from the measured velocities in the following manner:

$$a_w = \frac{1}{4mT}\int_{t_0}^{t_0+mT} \langle|\tilde{u}(t)|\rangle_z \,\mathrm{d}t. \tag{3.9}$$

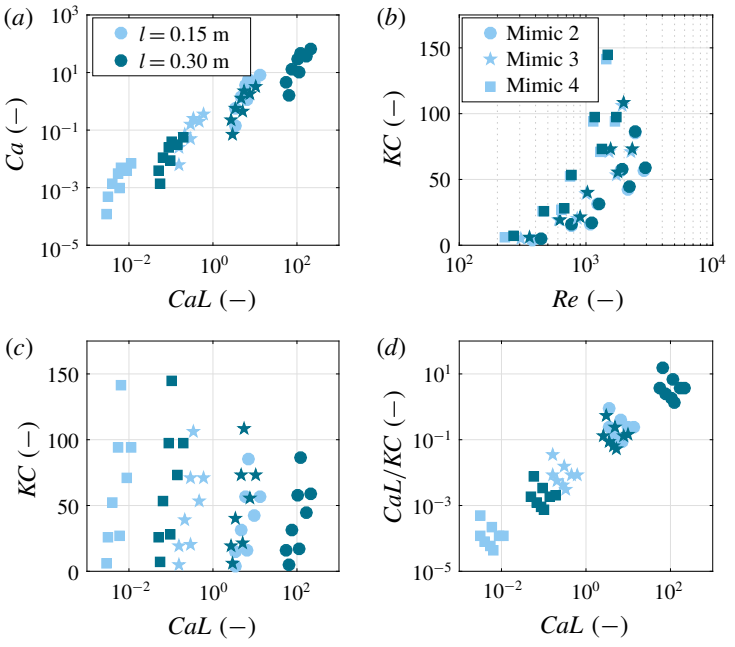

FIGURE 2. (Colour online) The range of non-dimensional parameters tested. Markers and colours have the same meaning in all panels.

This expression reduces to $a_w = u_w/\omega$ (linear wave theory), if $\tilde{u}$ is purely sinusoidal; m is an integer.

The values of a_w, u_w, $\langle \tilde{u}_c \rangle_z$, $\langle \tilde{u}_t \rangle_z$, $\langle \bar{u} \rangle_z$ are given in table 3 for all cases, and the quantities are evaluated for the part of the velocity signal that overlaps the video recordings; $\langle \tilde{u}_c \rangle_z$ and $\langle \tilde{u}_t \rangle_z$ are depth-averaged velocities evaluated under the crest and trough of the wave, respectively. It is seen that the two cases with $H = 0.04$ m and the case with $H = 0.07$ s and $T = 1.5$ s are almost sinusoidal, since the crest and trough velocities are practically identical. Higher harmonics in the velocity field are present for all other wave conditions. The significance is that a sinusoidal flow would result in a vanishing mean force on a rigid stem, but it will be described below how this is not the case for flexible stems.

Furthermore, the non-dimensional numbers: Reynolds ($Re = u_w \delta_y / \nu$), Keulegan–Carpenter (KC), Cauchy (Ca), L, CaL and CaL/KC are tabulated; $\nu = 10^{-6}$ m^2 s^{-1} is the kinematic viscosity of water. The non-dimensional parameters covered in this work are depicted in figure 2.

In summary, it is seen from table 3 and figure 2 that the ranges for Ca and CaL overlap each other for the three mimics; Ca is less than 0.01 for mimic 4, so it is effectively stiff, and no video recordings were made. The significance of CaL and CaL/KC for vegetation in waves was not identified upon design of the experiments, where Ca and KC were taken as the descriptive non-dimensional quantities. This is the reason that CaL has gaps over the full range, while Ca and KC do not.

3.3. *The motion of flexible stems*

3.3.1. *Example of stem motion*

Some examples of stem motion are depicted in figure 3. The depicted motion is based on ensemble averaging over multiple wave periods. The examples allow for a

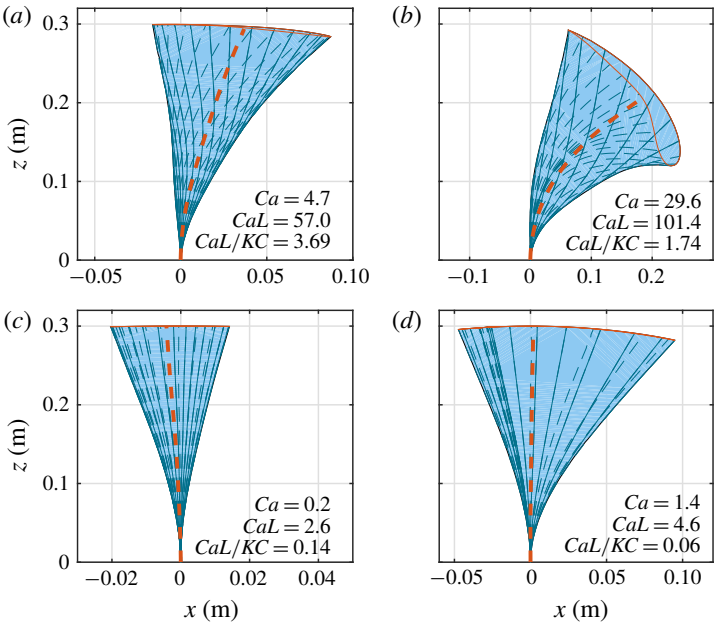

FIGURE 3. (Colour online) Four examples of single stem motion based on the ensemble-averaged displacement. All mimics have a length of $l = 0.30$ m. (*a*) Mimic 2, $H = 0.04$ m and $T = 2.0$ s. (*b*) Mimic 2, $H = 0.11$ m and $T = 3.0$ s. (*c*) Mimic 3, $H = 0.04$ m and $T = 2.0$ s. (*d*) Mimic 3, $H = 0.11$ m and $T = 3.0$ s. The full lines depict forward motion ($\partial x_s/\partial t > 0$) and dashed lines backward motion ($\partial x_s/\partial t$) of the tip. The time step between two lines is constant. The thick, dashed line is the mean position of the stem.

direct comparison of the effect of material and wave properties on the motion of a single stem. The sets of panels (*a*,*c*) and (*b*,*d*) each have the same $L = l/a_w$, so the difference of the motion is uniquely ascribed to the difference in material properties, which is captured by Ca and $CaL/KC \propto (T_n\omega)^2$, and a small difference in KC, due to a difference in δ_y between mimics. The stiffer the stem (the smaller Ca), the more upright it is.

The motion in figure 3(*a*) is clearly asymmetric, while the velocity field is almost sinusoidal (table 3). Since the hydrodynamic forcing is symmetric, the asymmetry is mainly attributed to the Lagrangian motion of the stem in a spatially varying velocity field, as discussed in Gijón Mancheño (2016). She discussed that the mean forward bending is attributed to the co-following of the tip of the stem under the crest, i.e. vaguely similar to Stokes drift. This effectively results in a mean force on the stem and an associated mean deflection.

The stem motion in figure 3(*c*) is backward asymmetric. The mean deflection of the stem was negative in stagnant water, which is why it is hypothesized that the plastic material had anisotropic properties and was pre-tensioned into a slightly curving form. It is deemed to have limited practical influence on the results. A comparison between panels (*c*,*d*) (same mimic) shows that the latter is forward asymmetric, thus a certain threshold of forcing had to be exceeded to overcome the hypothesized non-uniformity in the mechanical properties of the material.

The mean position of the stems is also plotted in figure 3 and a forward mean displacement is seen in panels (*a*,*b*). This finite mean displacement must be associated

Mimic	H (m)	T (s)	l (m)	a_w (cm)	u_w (cm s^{-1})	$\langle\bar{u}\rangle_z$ (cm s^{-1})	$\langle\tilde{u}_c\rangle_z$ (cm s^{-1})	$\langle\tilde{u}_t\rangle_z$ (cm s^{-1})	$Re \times 10^{-3}$ (−)	KC (−)	Ca (−)	L (−)	CaL (−)	CaL/KC (−)
2	0.04	1.0	0.15	0.6	3.8	0.1	3.8	−3.8	0.38	3.8	0.14	25.0	3.5	9.25×10^{-1}
3	0.04	1.0	0.15	0.6	3.8	0.1	3.8	−3.8	0.30	4.7	0.01	25.0	0.2	3.39×10^{-2}
4	0.04	1.0	0.15	0.6	3.8	0.1	3.8	−3.8	0.23	6.3	0.00	25.0	0.0	4.82×10^{-4}
2	0.04	1.0	0.30	0.7	4.4	−0.0	4.5	−4.4	0.44	4.4	1.55	42.4	65.9	1.48×10^{1}
3	0.04	1.0	0.30	0.7	4.4	−0.0	4.5	−4.4	0.36	5.6	0.07	42.4	3.0	5.42×10^{-1}
4	0.04	1.0	0.30	0.7	4.4	−0.0	4.5	−4.4	0.27	7.4	0.00	42.4	0.1	7.71×10^{-3}
2	0.04	2.0	0.15	2.4	7.6	−0.2	7.8	−7.2	0.76	15.2	0.57	6.2	3.5	2.31×10^{-1}
3	0.04	2.0	0.15	2.4	7.6	−0.2	7.8	−7.2	0.61	19.0	0.03	6.2	0.2	8.44×10^{-3}
4	0.04	2.0	0.15	2.4	7.6	−0.2	7.8	−7.2	0.46	25.4	0.00	6.2	0.0	1.20×10^{-4}
2	0.04	2.0	0.30	2.5	7.7	−0.2	8.0	−7.3	0.77	15.4	4.68	12.2	57.0	3.69×10^{0}
3	0.04	2.0	0.30	2.5	7.7	−0.2	8.0	−7.3	0.62	19.3	0.21	12.2	2.6	1.35×10^{-1}
4	0.04	2.0	0.30	2.5	7.7	−0.2	8.0	−7.3	0.46	25.7	0.00	12.2	0.0	1.92×10^{-3}
2	0.07	1.5	0.15	2.6	10.7	−0.6	10.9	−10.4	1.07	16.1	1.13	5.8	6.6	4.10×10^{-1}
3	0.07	1.5	0.15	2.6	10.7	−0.6	10.9	−10.4	0.86	20.1	0.05	5.8	0.3	1.50×10^{-2}
4	0.07	1.5	0.15	2.6	10.7	−0.6	10.9	−10.4	0.64	26.8	0.00	5.8	0.0	2.14×10^{-4}
2	0.07	1.5	0.30	2.7	11.2	−0.7	11.5	−10.8	1.12	16.7	9.77	11.3	110.2	6.59×10^{0}
3	0.07	1.5	0.30	2.7	11.2	−0.7	11.5	−10.8	0.89	20.9	0.45	11.3	5.0	2.41×10^{-1}
4	0.07	1.5	0.30	2.7	11.2	−0.7	11.5	−10.8	0.67	27.9	0.01	11.3	0.1	3.43×10^{-3}
2	0.07	2.5	0.15	4.9	12.4	−0.6	15.1	−9.8	1.24	31.1	1.52	3.1	4.6	1.49×10^{-1}
3	0.07	2.5	0.15	4.9	12.4	−0.6	15.1	−9.8	0.99	38.9	0.07	3.1	0.2	5.46×10^{-3}
4	0.07	2.5	0.15	4.9	12.4	−0.6	15.1	−9.8	0.75	51.8	0.00	3.1	0.0	7.76×10^{-5}
2	0.07	2.5	0.30	5.0	12.7	−0.7	15.6	−9.9	1.27	31.8	12.67	6.0	75.9	2.39×10^{0}
3	0.07	2.5	0.30	5.0	12.7	−0.7	15.6	−9.9	1.02	39.7	0.58	6.0	3.5	8.76×10^{-2}
4	0.07	2.5	0.30	5.0	12.7	−0.7	15.6	−9.9	0.76	52.9	0.01	6.0	0.1	1.25×10^{-3}
2	0.11	2.0	0.15	6.8	21.5	−1.4	24.4	−18.7	2.15	42.9	4.52	2.2	10.0	2.32×10^{-1}
3	0.11	2.0	0.15	6.8	21.5	−1.4	24.4	−18.7	1.72	53.6	0.21	2.2	0.5	8.51×10^{-3}
4	0.11	2.0	0.15	6.8	21.5	−1.4	24.4	−18.7	1.29	71.5	0.00	2.2	0.0	1.21×10^{-4}
2	0.11	2.0	0.30	7.0	22.0	−1.6	25.4	−19.1	2.20	44.1	38.13	4.3	164.3	3.73×10^{0}
3	0.11	2.0	0.30	7.0	22.0	−1.6	25.4	−19.1	1.76	55.1	1.75	4.3	7.5	1.37×10^{-1}
4	0.11	2.0	0.30	7.0	22.0	−1.6	25.4	−19.1	1.32	73.4	0.03	4.3	0.1	1.94×10^{-3}
2	0.11	3.0	0.15	8.6	18.9	−0.9	28.8	−12.3	1.89	56.8	3.51	1.7	6.1	1.08×10^{-1}
3	0.11	3.0	0.15	8.6	18.9	−0.9	28.8	−12.3	1.51	70.9	0.16	1.7	0.3	3.97×10^{-3}
4	0.11	3.0	0.15	8.6	18.9	−0.9	28.8	−12.3	1.14	94.6	0.00	1.7	0.0	5.64×10^{-5}
2	0.11	3.0	0.30	8.7	19.4	−1.0	29.8	−12.6	1.94	58.2	29.56	3.4	101.4	1.74×10^{0}
3	0.11	3.0	0.30	8.7	19.4	−1.0	29.8	−12.6	1.55	72.8	1.35	3.4	4.6	6.38×10^{-2}
4	0.11	3.0	0.30	8.7	19.4	−1.0	29.8	−12.6	1.16	97.0	0.03	3.4	0.1	9.07×10^{-4}
2	0.16	2.0	0.15	8.9	28.3	−2.5	34.2	−23.2	2.83	56.6	7.87	1.7	13.2	2.34×10^{-1}
3	0.16	2.0	0.15	8.9	28.3	−2.5	34.2	−23.2	2.27	70.8	0.36	1.7	0.6	8.56×10^{-3}
4	0.16	2.0	0.15	8.9	28.3	−2.5	34.2	−23.2	1.70	94.4	0.01	1.7	0.0	1.22×10^{-4}
2	0.16	2.0	0.30	9.2	29.2	−3.0	36.0	−23.7	2.92	58.4	66.99	3.3	219.5	3.76×10^{0}
3	0.16	2.0	0.30	9.2	29.2	−3.0	36.0	−23.7	2.34	73.0	3.07	3.3	10.0	1.38×10^{-1}
4	0.16	2.0	0.30	9.2	29.2	−3.0	36.0	−23.7	1.75	97.3	0.06	3.3	0.2	1.96×10^{-3}

TABLE 3. For caption see next page.

Mimic	H (m)	T (s)	l (m)	a_w (cm)	u_w (cm s^{-1})	$\langle\bar{u}\rangle_z$ (cm s^{-1})	$\langle\tilde{u}_c\rangle_z$ (cm s^{-1})	$\langle\tilde{u}_t\rangle_z$ (cm s^{-1})	$Re \times 10^{-3}$ (−)	KC (−)	Ca (−)	L (−)	CaL (−)	CaL/KC (−)
2	0.16	3.5	0.15	12.0	24.2	−1.4	39.7	−17.6	2.42	84.9	5.77	1.2	7.2	8.50×10^{-2}
3	0.16	3.5	0.15	12.0	24.2	−1.4	39.7	−17.6	1.94	106.1	0.26	1.2	0.3	3.11×10^{-3}
4	0.16	3.5	0.15	12.0	24.2	−1.4	39.7	−17.6	1.45	141.5	0.01	1.2	0.0	4.43×10^{-5}
2	0.16	3.5	0.30	12.1	24.8	−1.7	41.4	−17.8	2.48	86.7	48.20	2.5	119.1	1.37×10^{0}
3	0.16	3.5	0.30	12.1	24.8	−1.7	41.4	−17.8	1.98	108.4	2.21	2.5	5.5	5.03×10^{-2}
4	0.16	3.5	0.30	12.1	24.8	−1.7	41.4	−17.8	1.49	144.5	0.04	2.5	0.1	7.16×10^{-4}

TABLE 3. An overview of the characteristic wave parameters and the corresponding non-dimensional parameters relevant for the motion of the stem and force coefficients.

with a mean force on the stems, so an equally large mean force is acting on the water column. The increase in hydrodynamic forcing gives a significant increase in tip displacement for mimic 3 (panels *c*,*d*), while a relatively smaller increase in tip displacement for mimic 2 under the same forcing. This is attributed to the larger mean displacement of the stem in panel (*b*), which limits the allowed oscillatory displacement from the mean. It is seen below that the mean displacement complicates a unified description of the stem motion.

Proper orthogonal decompositions (see appendix C) of the four examples are shown in figure 4. It is seen that the motion of mimic 3 is described by the mean and a single mode, while the displacement of mimic 2 also requires a second mode for an accurate description. This is in line with the prediction by Leclercq & De Langre (2018), who give an upper limit of $CaL/KC = 0.20$ for the static regime. The static regime is defined as the quasi-static equilibrium between the internal elastic force and the hydrodynamic forcing, so only one mode shape is required.

Four videos of the examples in figures 3 and 4 supplement this paper, see appendix D.

3.3.2. *Motion characteristics*

The results presented above show that there is a trend for the stem to be increasingly forward asymmetric when the value of Ca or CaL increases. The variation with CaL/KC is less intuitive for understanding the displacements (figure 3), but useful in understanding the relevance of a second mode shape (figure 4).

Some measures of the horizontal stem position, x_s, are investigated in this section: $\max\langle\tilde{x}_s\rangle$, $\min\langle\tilde{x}_s\rangle$, $\Delta\langle\tilde{x}_s\rangle$ and $\overline{\langle x_s\rangle}$. Here, $\langle\rangle$ denotes ensemble averaging and $\langle\tilde{x}_s\rangle = \langle x_s\rangle - \overline{\langle x_s\rangle}$. The displacements are made non-dimensional with a_w in accordance with choice in § 3.1. The results are plotted as a function of CaL in figure 5 and CaL/KC in figure 6, where x_s is taken at the tip of the stem. A few of the data points are marked with a white dot to indicate that $0.5 < \overline{\langle x_s\rangle}/l$, i.e. the mean tip displacement exceeds 50 % of the stem length. A large mean deflection will be seen to limit the magnitude of oscillatory displacements, because the tip displacement cannot exceed 100 % of the stem length.

The first observation is that CaL/KC describes the overall behaviour considerably better than CaL if the data points with large mean displacement are neglected; see the white dots. The difference is most noticeable in the range $CaL \in [2, 20]$ and $CaL/KC \in [0.05, 1]$, where the data exhibit much less vertical scatter as a function of CaL/KC. Data points for both mimic 2 with $l = 0.15$ m and mimic 3 with $l = 0.30$ m overlap in these parameter intervals, but only CaL/KC leads to a collapse

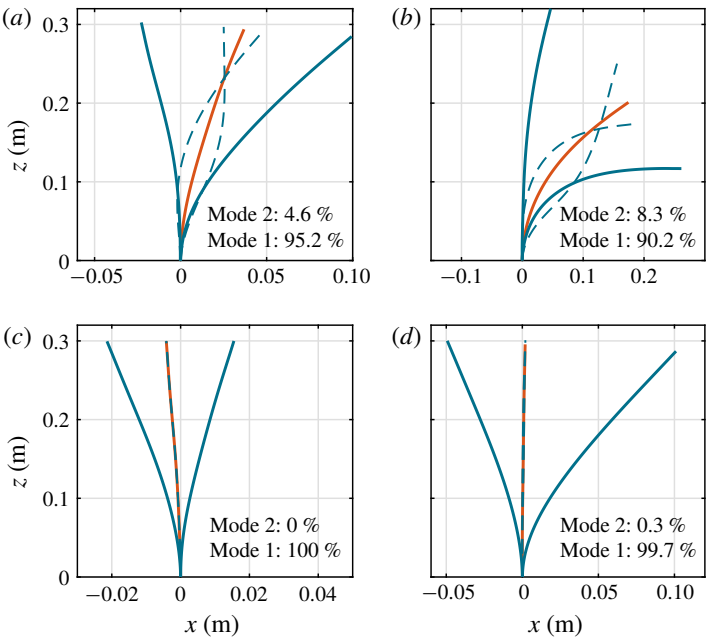

FIGURE 4. (Colour online) Four examples of single stem motion decomposed into proper orthogonal decomposition (POD) modes. All mimics have a length of $l = 0.30$ m. (*a*) Mimic 2, $H = 0.04$ m and $T = 2.0$ s. (*b*) Mimic 2, $H = 0.11$ m and $T = 3.0$ s. (*c*) Mimic 3, $H = 0.04$ m and $T = 2.0$ s. (*d*) Mimic 3, $H = 0.11$ m and $T = 3.0$ s. Red line, mean displacement. Full blue line, mode 1. Dashed blue line, mode 2. The percentage describes the importance of the mode for the time varying motion.

of the data. This means that the natural period ($CaL/KC \propto (T_n\omega)^2$) is more important than the drag force exerted on the stem; the latter scaling with CaL in (3.2). The magnitude of the hydrodynamic forcing, incorporated by normalizing with a_w, is also justified. It is seen that $\Delta\langle\tilde{x}_s\rangle/a_w$ reaches values of 4.0, so the acceleration of the stem tip exceeds that of the water and the inertia force on the stem retards the tip displacement under these conditions (see also supplementary video material available at https://doi.org/10.1017/jfm.2019.739 and appendix D). Consequently, the investigated stems seem to have an upper allowed acceleration, because of the added mass effect. Leclercq & De Langre (2018), in their figure 4, showed that the tip displacement converged to a asymptotic value of $\max x_s/l \simeq 0.45$ for $a_w/l = 0.27$ for increasing ω. The ratio $\max x_s/a_w = 0.45/0.27 = 1.67$, a similar result as in the present study. Mimics 2 and 3 had a sufficiently large torsional stiffness to suppress torsional motion, while mimic 1 (otherwise not analysed here) showed a large degree of torsion during phases of large acceleration, thereby reducing the effect of added mass.

The general picture is that there is no noticeable displacement of the stem up to approximately $CaL = 1.0$, so at least the stem behaves as effectively rigid up to this value (see figure 5). This is in line with figure 5 in Luhar & Nepf (2011) and figure 11 in Luhar & Nepf (2016), who investigated the concept of effective length for pure current and waves, respectively.

For larger displacements, the displacements increase with increasing CaL/KC, yet still with close to vanishing mean displacements up to $CaL/KC = 0.8$ (figure 6). For

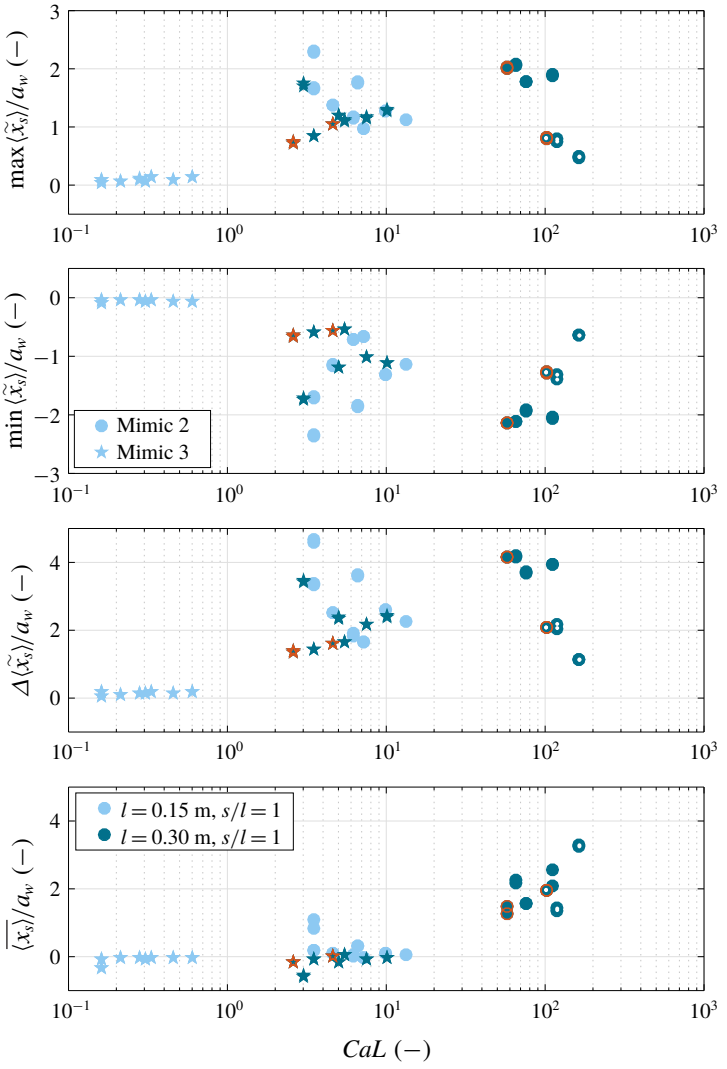

FIGURE 5. (Colour online) Characteristic measures of the motion of the tip of the stem as a function of CaL. The data are for mimics 2 and 3. The red markers correspond to the cases depicted in figure 3. The white dots indicate cases with $0.5 < \overline{\langle x_s\rangle}/l$.

$CaL/KC > 0.8$, $\max\langle x_s\rangle/a_w$ and $|\min\langle x_s\rangle|/a_w$ show some scatter in the range 0.5–2.0. The cases with values different from approximately 2 related to a large value of $\overline{\langle x_s\rangle}/l$, i.e. most of the deflection potential is already taken by the mean deflection (shown as white dots).

It was investigated whether a better representation of the data could be achieved by normalizing with l instead of a_w, e.g. in line with the choice by Luhar & Nepf (2016) and Leclercq & De Langre (2018). The results conclusively showed that a_w is the better horizontal length scale of the two. The non-dimensional scaling adopted in the present work appears applicable to the description of flexible stems with small mean deflections.

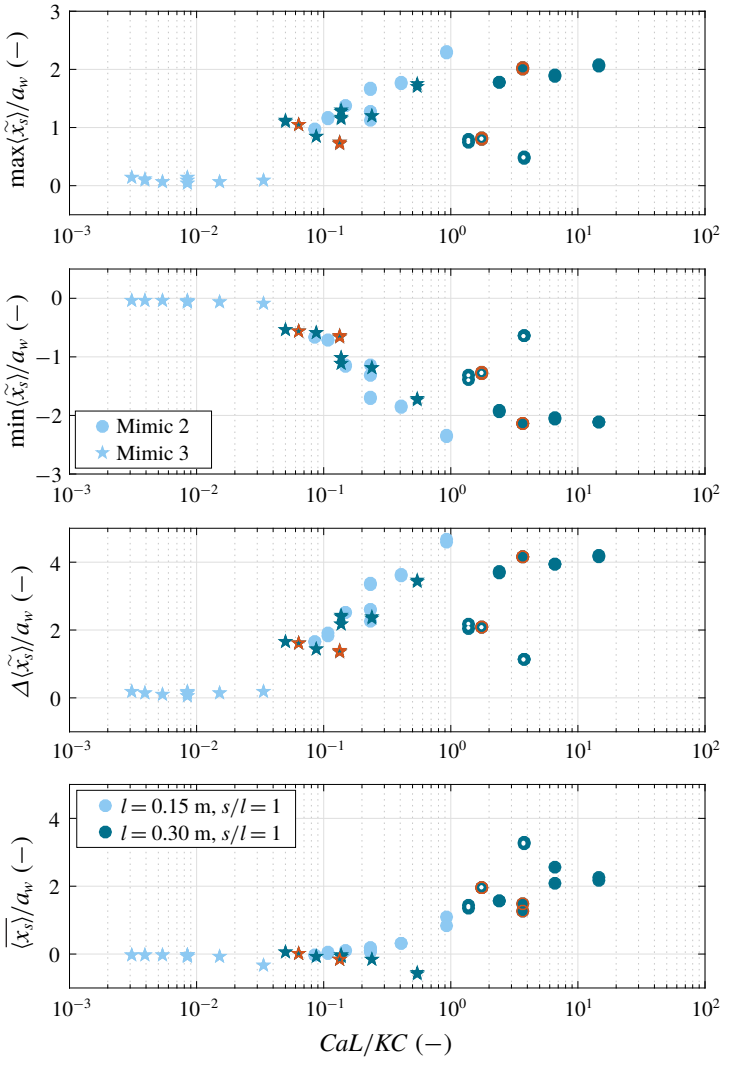

FIGURE 6. (Colour online) Characteristic measures of the motion of the tip of the stem as a function of $CaL/KC \propto (T_n\omega)^2$. The data are for mimics 2 and 3. The red markers correspond to the cases depicted in figure 3. The white dots indicate cases with $0.5 < \overline{\langle x_s \rangle}/l$.

3.3.3. *Phase lags*

The fluid and stem motions are not necessarily in phase, which was described theoretically and verified against field measurements for weakly flexible vegetation (Mullarney & Henderson 2010). The large flexibility in the present experiments (e.g. figure 3*b*) and the presence of a second mode shape (figure 4*b*) mean that the phase lag is not constant along the stem. This is easily seen in figure 3(*b*), where the tip of the stem reaches an extreme forward position later than any point below the inflection point at $z \simeq 0.1$ m. The tracking algorithm and the synchronization with the velocity field allow for an evaluation of this phase lag. All cases where the tip was displaced more than 3 mm (7.5 pixels) were included in the analysis. Cases with smaller tip displacements were too noisy for accurate estimates.

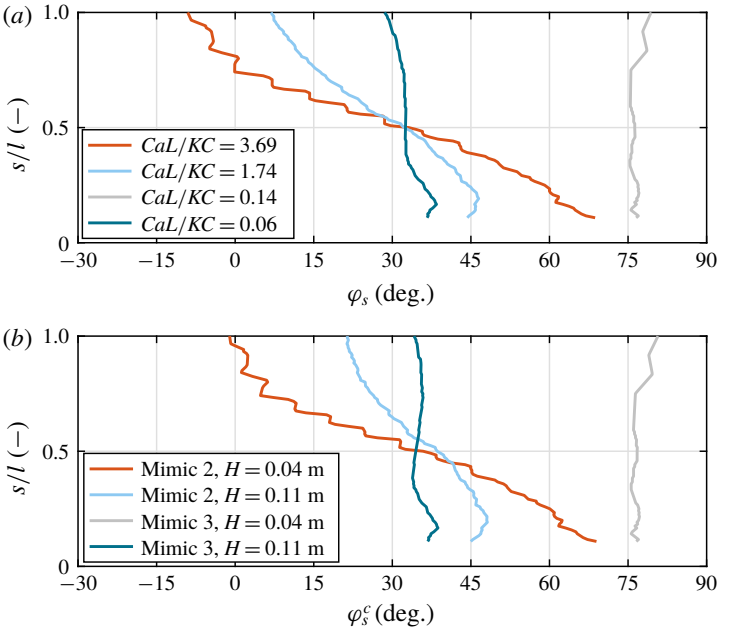

FIGURE 7. (Colour online) The variation of φ_s (*a*) and φ_s^c (*b*) over the length of the stem. The lines match panels (*a–d*) in figure 3. $l = 0.30$ m.

Two phase lags were defined,

$$\varphi_s(s/l) = \frac{360^\circ}{T}(t_{u=max\,x_w} - t_{x_s=max\,x_s}) \tag{3.10}$$

and

$$\varphi_s^c(s/l) = \varphi_s(s/l) - \frac{360^\circ}{T}\frac{\max x_s}{c}, \tag{3.11}$$

where x_w is the water particle position, c is the wave celerity and s is a local coordinate along the length of the stem with $s/l = 0$ at the base of the stem and $s/l = 1$ at the tip. Equation (3.10) defines the phase lag between the instances at which x_s is maximum and the time at which the fluid particle position (x_w) is maximum (evaluated at $x = 0$ m). Here, φ_s^c accounts for the fact that the stem reaches its maximum position for $x > 0$ m, so it experiences a different velocity field than at $x = 0$. The fluid particle position is evaluated as

$$x_w(t) = \int_0^t \tilde{u}(\tau)\,\mathrm{d}\tau, \tag{3.12}$$

where φ_s and φ_s^c are plotted over the length of the stem (figure 7) for the four examples shown in figure 3. The results are plotted for $s/l > 0.1$. Generally, the phase lag for mimic 2 has a gradually decreasing value of φ_s over the length of the stem. For the stiffer mimic 3 with $CaL/KC < 0.2$, φ_s is practically constant over the length of the stem. It is seen that the behaviour is qualitatively identical for φ_s and φ_s^c, but differences of 15° are observed. The vertical variation in φ_s^c for mimic 2 is

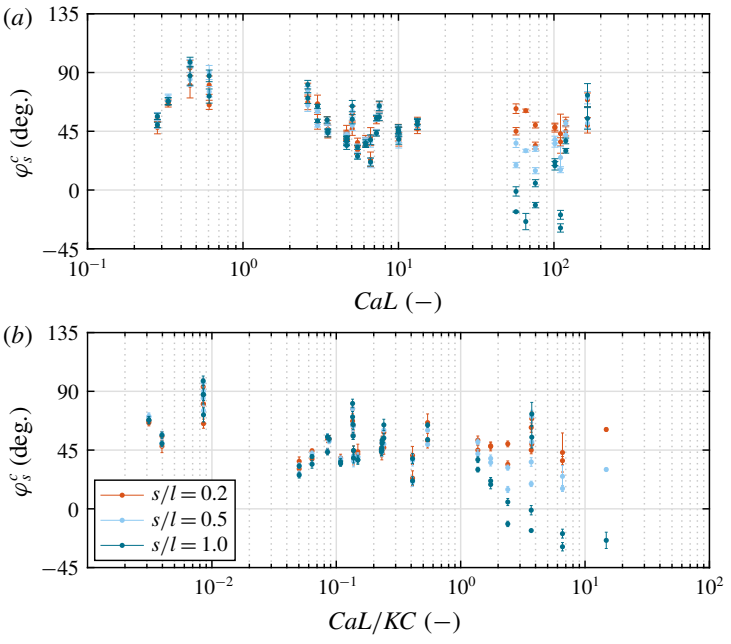

FIGURE 8. (Colour online) The phase lag between the maximum fluid particle displacement and the maximum displacement of the stem, φ_s^c. The error bars show the $\pm\sigma$ range, where σ is the standard deviation. (*a*) The quantities are plotted as a function of CaL. (*b*) The quantities are plotted as a function of CaL/KC.

attributed to the finite amount of energy on the second mode shape, while there is no energy on the second mode shape for mimic 3, so the phase lag is constant.

In figure 8, φ_s^c is depicted for three points along the stem ($s/l = \{0.2, 0.6, 1.0\}$) as a function of CaL and CaL/KC, respectively. Values of φ_s^c are found per wave period and the mean and the standard deviation are calculated. Neither of the two parameters CaL and CaL/KC gives a convincing relationship with the phase lag. Nonetheless, it is seen that all points along the stem have the same phase up to $CaL < 20$ and $CaL/KC < 0.5$, so the stem shape must be described fully by a single mode shape. The limit of $CaL/KC \simeq 0.5$ corresponds fairly well with the theoretical limit of transition away from the static regime proposed by Leclercq & De Langre (2018) (see § 3.1).

3.3.4. *Relative velocities and accelerations*

The relative velocities and accelerations between the orbital velocities and the stem motion are evaluated in order to describe the motion, but also to evaluate the force coefficients. The relative velocities and accelerations are defined as follows:

$$u_r^c|_t = u|_{t-\Delta t_s} - \left.\frac{\partial x_s}{\partial t}\right|_t \quad \text{and} \quad \left.\frac{\partial u_r^c}{\partial t}\right|_t = \left.\frac{\partial u}{\partial t}\right|_{t-\Delta t_s} - \left.\frac{\partial^2 x_s}{\partial t^2}\right|_t. \tag{3.13a,b}$$

Here, Δt_s is x_s/c and superscript c is used to indicate the Lagrangian correction. The offset is introduced because the stem does not experience the velocity measured by the EMF at $x = 0$ m. Therefore, when $x_s > 0$ m, the stem is exposed to a velocity that has already been recorded at $x = 0$ m. Similarly, the stem is exposed to velocities yet to be recorded, when $x_s < 0$ m. Similar expressions hold for w_r and $\partial w_r/\partial t$. The

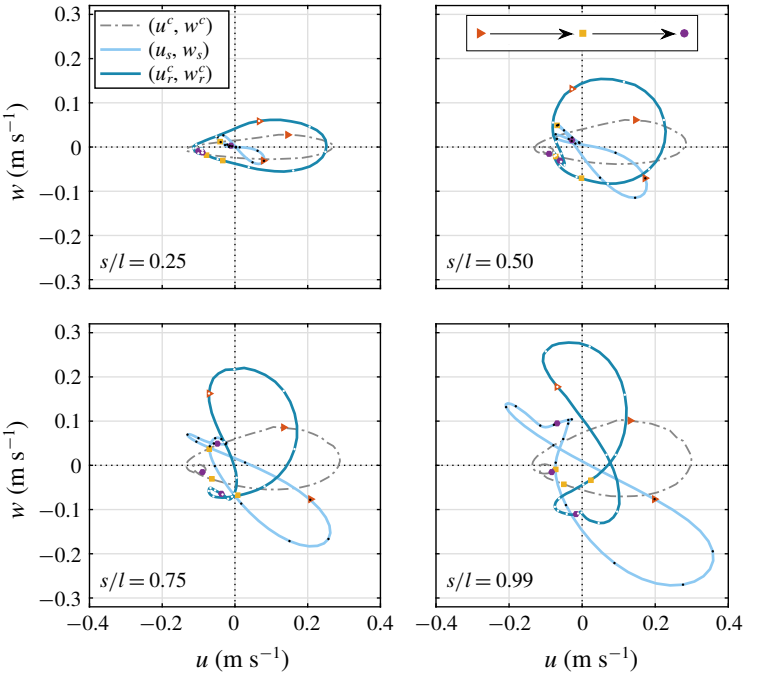

FIGURE 9. (Colour online) Lissajous curves for (u^c, w^c), (u_s, w_s) and (u_r^c, w_r^c). Lines are ensemble averages. The small black/white dots on the curves mark time with a spacing of 0.2 s. The coloured markers indicate the direction of the temporal axis. Mimic 2, $l = 0.30$ m, $H = 0.11$ m and $T = 3.0$ s. The aspect ratio is 1.0:0.8.

velocity and acceleration of the stem segments are evaluated with proper orthogonal decomposition of the stem motion and algebraic differentiation (appendix C), while the temporal derivatives of u and w are based on a simple central finite difference scheme.

The orbital, stem and relative velocities are depicted in the following with Lissajous curves (see figures 9 and 10). Here, u is plotted along the horizontal axis and w along the vertical axis. Lissajous curves form an ellipse when u and w are 90° out of phase, while the curve forms a line when u and w are in phase; (u^c, w^c) can be seen as a closed curve, but the nonlinearity in the wave has shifted the curve towards the right and $w^c \neq \max w^c$ when $u^c = 0$.

The curves in figures 9 and 10 are depicted for four points along the length of the stem. The figures correspond to panels (*b*) (mimic 2) and (*d*) (mimic 3) in figure 3 and the only difference between the two sets of Lissajous curves is the stem properties ($H = 0.11$ m, $T = 3/0$ s and $l = 0.30$ m). A comparison between the two figures shows that $-\min u_s < \max u_s$ for mimic 2, while $\max u_s < -\min u_s$ for mimic 3, i.e. either the forward or backward velocity is the largest. The more flexible stem (smaller EI) readily follows the flow, while the stiffer stem (larger EI) 'shoots' backward as soon as the hydrodynamic loading decreases. This is caused by the elastic energy stored in the stem during the forward motion (see also theoretical analysis in Mullarney & Henderson 2010).

The figures show that u_r^c is generally larger in the positive direction and the curve (u_r^c, w_r^c) follows a relatively simple closed curve for $s/l < 0.5$. The pattern is more

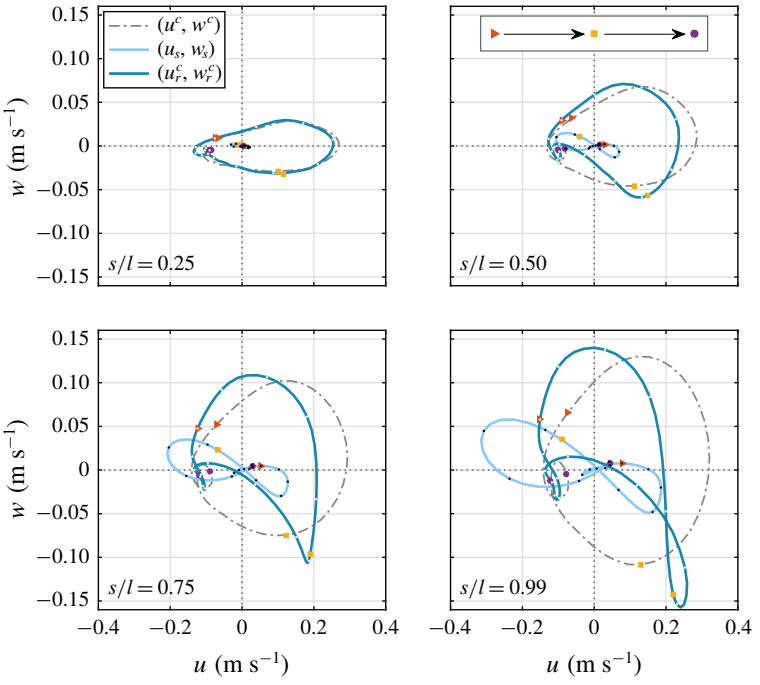

FIGURE 10. (Colour online) Lissajous curves for (u^c, w^c), (u_s, w_s) and (u_r^c, w_r^c). Lines are ensemble averages. The small black/white dots on the curves mark time with a spacing of 0.2 s. The coloured markers indicate the direction of the temporal axis. Mimic 3, $l =$ 0.30 m, $H = 0.11$ m and $T = 3.0$ s. The aspect ratio is 1.0:0.4.

complex higher on the stem ($0.5 < s/l$). The fluid velocity governs the hydrodynamic loading at the base of the stem, since $u_s \ll u_r^c$ and $u_r^c \simeq u$. At the tip of the stem, the combined stem velocity and phase difference results in a lowering of u_r^c, so the hydrodynamic loading at the tip is expected to be smaller than at the bed (figure 9).

Finally, it is seen for both mimics that $\max|u_r^c| < \max|u^c|$, while $\max|w^c| < \max|w_r^c|$ for mimic 2 and $\max|w_r^c| < \max|w^c|$ for mimic 3. Consequently, the flexibility of the stem is expected to reduce the inline force. However, the vertical motion can cause vertical tip velocities of the same order of magnitude as the horizontal, so a flexible stem may still be subject to large forces in waves. How the vertical force transfers to the root cannot be evaluated in this work, since a one-dimensional force transducer was used. Nonetheless, given the large positive vertical velocity, an uprooting force is expected.

3.4. *Average force coefficients*

The average force coefficients C_D and C_M are derived for mimics 2, 3 and 4. The force coefficients are normally calculated based on a least-square method (e.g. Sumer & Fredsøe 1999) with a representative velocity and acceleration. In the present case, the stem moves in the fluid and thereby changes its exposed area to the flow. This is illustrated in figure 11, where the maximum, F_c, and minimum, F_t, forces at the base are compared for stem lengths $l = 0.15$ m and $l = 0.30$ m and identical conditions. F_c and F_t were found with a zero-crossing analysis on the force time series. The

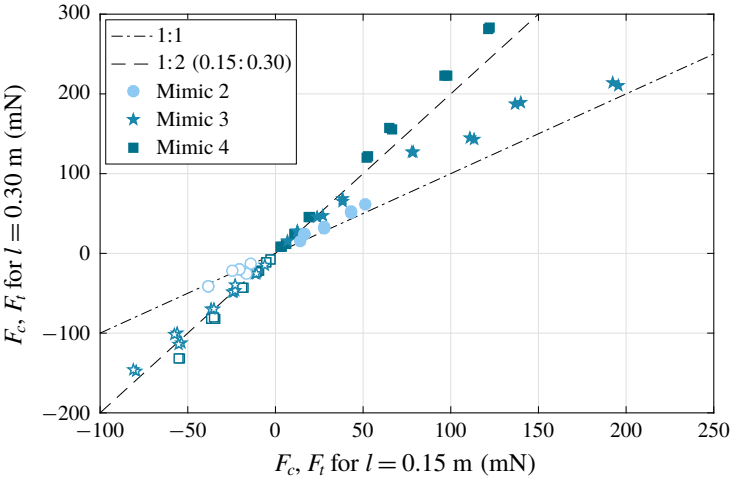

FIGURE 11. (Colour online) The measured peak forces for mimics 2, 3 and 4. The minimum force, F_t, is shown with empty markers and the maximum force, F_c, with filled markers.

forces for mimic 4 are approximately a factor of 2 larger for $l = 0.30$ m than for $l = 0.15$ m, while the forces do not scale linearly with l for mimics 2 and 3. The more the doubling from 0.15 m to 0.30 m for mimic 4 is due to the increase of orbital velocity with the distance from the bed; F_t shows a factor of 2 increase for both mimics 3 and 4, which is attributed to the fact that the stem is more upright under the wave trough than under the wave crest. The results for mimic 3 suggest that the exposed length of the stem varies over one wave period, so the instantaneous shape of the stem should be accounted for, when the force coefficients are evaluated.

The force coefficients are found by integration of (3.1) along the instantaneous shape of the stem,

$$F_x = \int_0^l EI\frac{\partial^4 x_s}{\partial z^4}\,\mathrm{d}s = \rho\delta_x\delta_y\int_0^l\left(\frac{\partial u^c}{\partial t} - \frac{\rho_s}{\rho}\frac{\partial^2 x_s}{\partial t^2}\right)\mathrm{d}s + \rho C_M\frac{\pi\delta_y^2}{4}\int_0^l\frac{\partial u_r^c}{\partial t}\cos\theta_s\,\mathrm{d}s + \frac{1}{2}\rho C_D\delta_y\int_0^l u_r^c\sqrt{u_r^{c,2}+w_r^{c,2}}\cos\theta_s\,\mathrm{d}s, \tag{3.14}$$

where F_x is the force at the base. Here, $\cos\theta_s$ accounts for the effective length of a stem segment and θ_s is the angle of the stem from the vertical; θ_s varies along the length of the stem. Note that the Lagrangian correction to the relative velocities and accelerations is used, but it only matters for a few of the conditions with large CaL/KC. All properties in (3.14) are measured, so a least-squares approach can be used to calculate C_M and C_D. The Froude–Krylov and inertia terms are explicitly accounted for, but they only affect the value of C_M for mimic 4 with $\delta_y = \delta_x$.

The values of C_M and C_D are plotted as a function of KC in figure 12(*a*,*b*), where C_M shows considerable scatter and there does not seem to be any organized trend when looking at individual mimics or individual values of l. This is attributed to the limited importance of the inertia force in the present experiments for $KC > 10$ and the fact that a part of the stem experiences large velocities at a given instance, while another part experiences large relative accelerations (for the more flexible stems). The

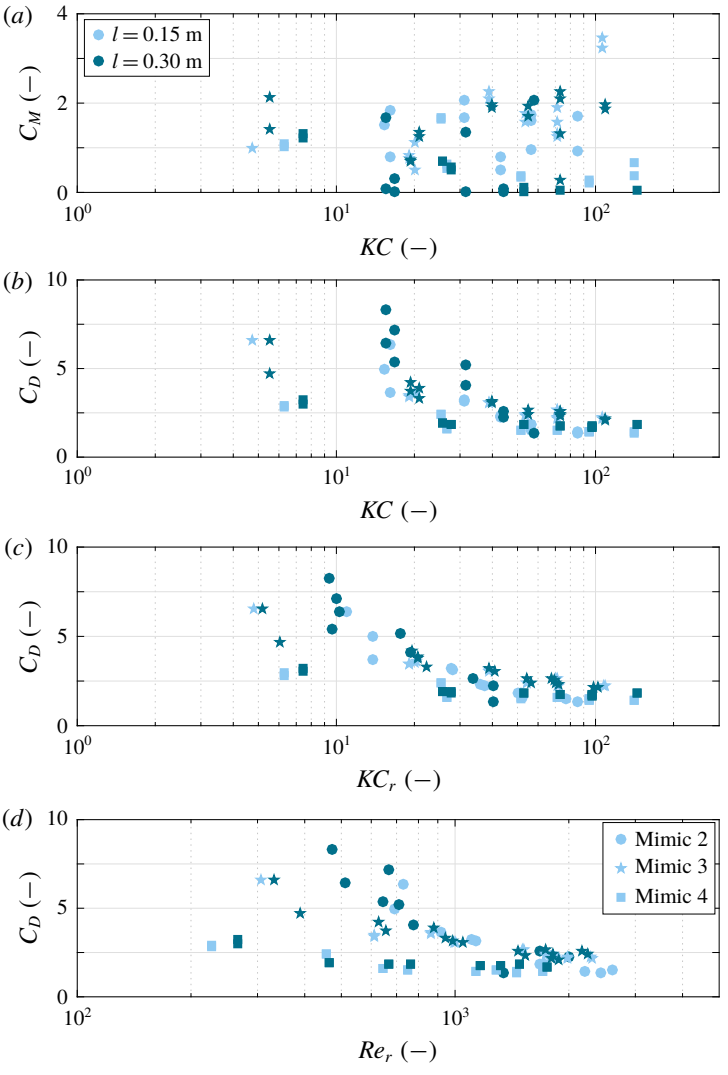

FIGURE 12. (Colour online) The average force coefficients for mimics 2, 3 and 4. (*a*) The inertia coefficient C_M as a function of KC. (*b*) The drag coefficient C_D as a function of KC. (*c*) C_D as a function of KC_r. (*d*) C_D as a function of Re_r.

value of C_D shows less scatter as a function of KC than C_M, but there are still clusters with separate trend curves: (i) $KC < 10$; (ii) $10 < KC < 30$; (iii) $30 < KC$.

The definition of KC (3.3) is based on the fluid velocity, while the stem experiences the relative velocity. Therefore, the relative Keulegan–Carpenter and Reynolds numbers were defined as

$$KC_r = \frac{2\pi u^c_{w,r}}{\omega \delta_y} \quad \text{and} \quad Re_r = \frac{u^c_{w,r}\delta_y}{\nu}, \tag{3.15a,b}$$

where

$$u^c_{w,r} = \sqrt{2}\left\langle \sqrt{\overline{(u^c_r - \bar{u}^c_r)^2}} \right\rangle_z . \tag{3.16}$$

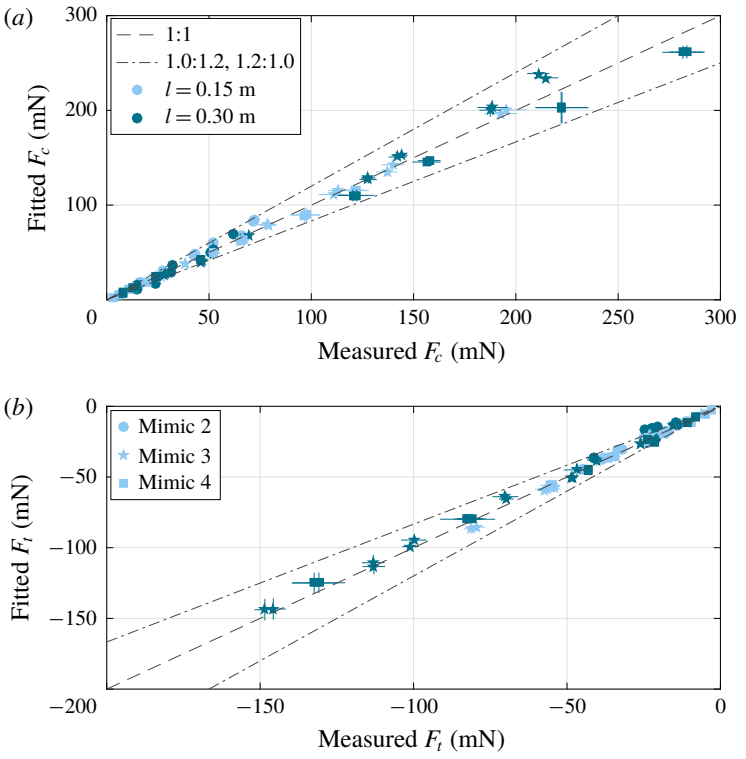

FIGURE 13. (Colour online) Comparison between the measured and fitted forces for all mimics (2, 3 and 4). Markers show the mean value and the lines show the standard deviation. The standard deviation is shown for both measured and fitted values. (*a*) The maximum force, F_c. (*b*) The minimum force, F_t. Dashed line, 1:1 fit. Dash-dotted lines, 1:1.2 and 1.2:1 fits.

The value of C_D is depicted as a function of KC_r and Re_r in figure 12(*c*,*d*). The change from KC to KC_r mostly affects KC for mimic 2, but it is enough to merge the two separate trends for $10 < KC$; C_D shows less scatter as a function of Re_r than Re (the latter not depicted) and CD decreases with increasing Re_r.

There seem to be a separation of C_D for the three mimics for low values of KC_r and Re_r. The increase in C_D with decreasing Re_r and KC_r is commonly known and is due to the omission of viscous effects in the drag (e.g. Sumer & Fredsøe 1999). Inclusion of a linear drag term was attempted, but due to the partial correlation between $u_r^c|u_r^c|$, u_r^c and $\partial u_r^c/\partial t$, the least-squares system provided poor results and a direct evaluation of linear and nonlinear drag coefficients was not achieved.

It was confirmed that the force coefficients (C_D and C_M) are not a function of either Ca, CaL or CaL/KC. This makes sense, because the force coefficients represent the interaction between stem and fluid, and they should not be a direct function of the mechanical properties of the stem.

The accuracy of the fitting is presented in figure 13, where the mean and standard deviation of F_c and F_t are presented for both measured and fitted values. It is seen that the fitted loads are captured accurately and generally within 10 %–20 % of the measured force. The mean deviation over all data sets is 2 %.

3.5. *Distribution of the external and internal forces along the stem*

The estimated average force coefficients allow for an evaluation of the force distribution, f_x, along the length of the stem. The force distribution subsequently allows for an approximate distribution of the internal shear force, V_x, within the stem as follows:

$$V_x(s) = \int_s^l f_x \, \mathrm{d}s, \tag{3.17}$$

where $V_x(s)$ is only an approximation, because the force coefficients for vertical forces on the stem could not be derived.

An example is shown in figure 14 for mimic 3 with $H = 0.04$ m, $T = 2.0$ s and $l = 0.30$ m (corresponding to figure 3*c*). The stem only experiences small displacements and the total force and the inertia are seen to be out of phase (compare panels *a*,*b*). The inertia force contributes less than 10 % to the maximum distributed force. It can also be seen that the maximum loading on the stem takes place at the base of the stem and at the tip of the stem. The latter due to the large relative velocities at the tip of the stem and for the former because $u_r^c = u^c$ at the base. Finally, panel (*c*) shows V_x, which changes in a monotonic fashion from the tip towards the base of the stem. Unless there are local weaknesses, the stem is most likely to break at the base or become uprooted.

Another example is shown in figure 15 for mimic 2 with $H = 0.04$ m, $T = 2.0$ s and $l = 0.30$ m (corresponding to figure 3*a*). This case differs from the above: (i) the displacements are larger. (ii) The phase lag over the length of the stem is not a constant (figure 7). It is clear to see that there are considerable temporal shifts in the maximum distributed force over the length of the stem, which is attributed to the fact that φ_s^c varies from 75° at the base to 0° at the tip of the stem. The distributed force vanishes at $s/l = 0.70$ over the entire wave period. The inertia force shows a similar temporal shift; again attributed to φ_s^c. The inertia force contributed 10 %–15 % of the maximum force.

Finally, figure 15(*c*) shows V_x, where oblique lines for $V_x = 0$ mN are seen as a function of time. This is opposite to the example with mimic 3, where $V_x = 0$ mN over the entire length of the stem at a given time instance. This effectively means that the force at the base only receives contributions from the lower part of the stem, which is approximately half the stem in the present case. Furthermore, while the maximum of $|V_x|$ still takes place at the base, there are almost as large values of $|V_x|$ along the upper half of the stem (approximately 70 % of the maximum base force). The maximum in V_x at $z/l = 0.75$ occurs almost simultaneously with the minimum in V_x at the base of the stem. Consequently, it is not unlikely that the stem will break away from the root, if the stem is already damaged.

The differences in internal shear stresses for the two examples are linked to the presence of a second mode shape for mimic 2 (see figure 4*a*,*c*). Mimic 3 falls in the static regime (Leclercq & De Langre 2018) which explains the monotonic behaviour. The second mode shape for mimic 2 is seen to directly influence the shear distribution in the stem.

It was mentioned in conjunction with the Lissajous curves in figure 9 that the distributed force along the stem for mimic 2 with $H = 0.11$ m, $T = 3.0$ s and $l = 0.30$ m would be maximum below the tip (the relative velocity is largest below the tip). Plots similar to figures 14 and 15 were made and it was indeed observed that the force ranges from −120 to 500 mN at the base of the stem, while the force at the tip of the stem only ranges from −120 to 200 mN. The force at the stem has

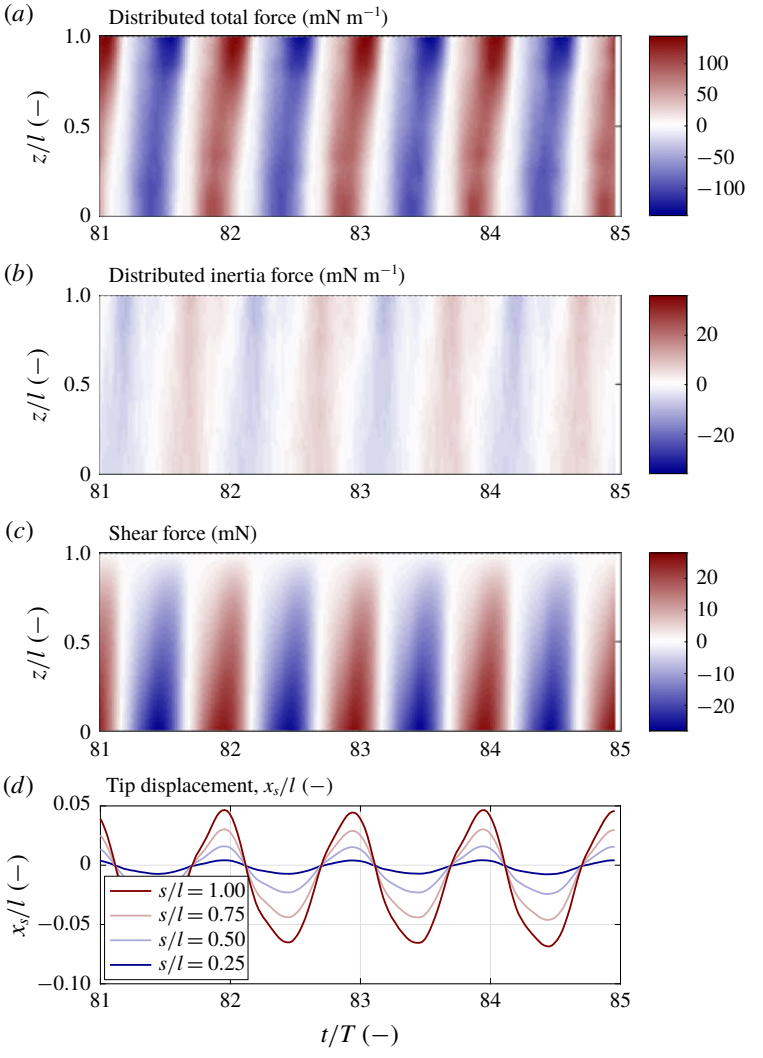

FIGURE 14. (Colour online) (*a*) The distributed total force in mN m^{-1} as a function of space and time. (*b*) The distributed inertia force in mN m^{-1} (total subtracted drag). (*c*) An estimate of the internal shear force in mN. (*d*) x_s/l at four points along the stem. Mimic 3, $l = 0.30$ m, $H = 0.04$ m, $T = 2.0$ s and the stem motion is that of figure 3(*c*).

a wide trough and a narrow and high peak and V_x shows a limited temporal shift, see figure 16.

The supplementary video material (appendix D) shows the distributed hydrodynamic force and the internal shear force.

3.6. *Summary*

The results have shown that the classification by Leclercq & De Langre (2018) based on the ratio of the natural period to the wave period ($T_n\omega$) can be extended to flexible stems in real waves. It is also seen that the main non-dimensional parameters $T_n\omega$ and CaL/KC (derived in this work) are equivalent. The motion of the stems can be

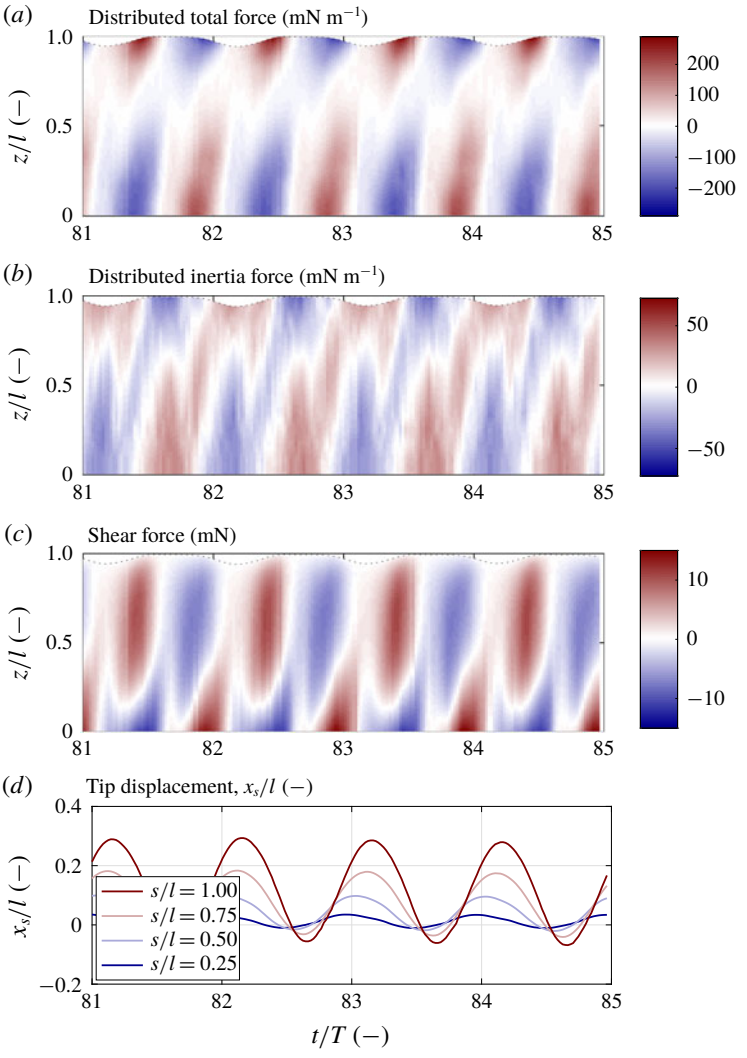

FIGURE 15. (Colour online) (*a*) The distributed total force in mN m^{-1} as a function of space and time. (*b*) The distributed inertia force in mN m^{-1} (total subtracted drag). (*c*) An estimate of the internal shear force in mN. (*d*) x_s/l at four points along the stem. Mimic 2, $l = 0.30$ m, $H = 0.04$ m, $T = 2.0$ s and the stem motion is that of figure 3(*a*).

subdivided into two aspects: (i) shape and (ii) magnitude. The results presented in § 3.3.2 suggest that the magnitude scales better with a_w than l; the former selected in the present work as the non-dimensional, horizontal length scale. The shape is described by CaL/KC, which effectively informs on the possibility that the motion of the stem will trigger higher mode shapes.

The existence of a second mode shape gives rise to a non-uniform phase lag along the length of the stem (§ 3.3.3). The second mode shape also gives rise to more complicated relative velocities and accelerations and a maximum in the internal shear force away from the stem (§ 3.5). Consequently, the existence of more than a single mode shape can be used to predict whether a stem will break at the base of the stem

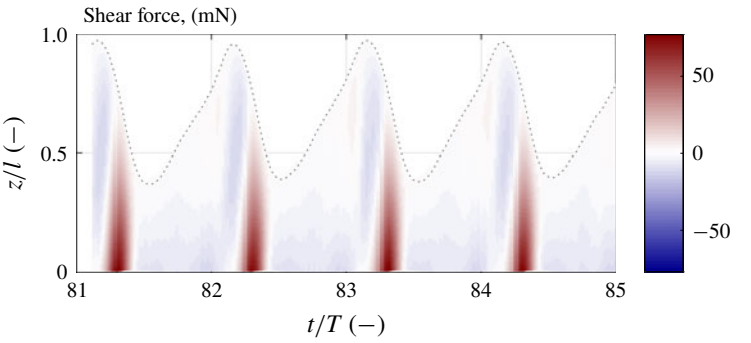

FIGURE 16. (Colour online) An estimate of the internal shear force in mN. Mimic 2, $l = 0.30$ m, $H = 0.11$ m, $T = 2.0$ s and the stem motion is that of figure 3(*b*).

or higher up: the smaller the value of $CaL/KC \propto (T_n\omega)^2$, the more likely it is that the stem will break at the base.

4. Discussion of canopy scale processes

Extrapolation of the motion characteristics of an individual stem to the characteristics of canopies is not necessarily possible. The presence of a canopy introduces a mean flow within and above the canopy (e.g. Luhar *et al.* 2010), where the most pronounced feature is a streaming-like mean current at the top of the canopy. The mean current will result in an increased mean deflection of the stems and thereby reduce the magnitude of the transient part of the motion. This is also seen experimentally in Lei & Nepf (2019), who compared motion of a single stem with the motion in a canopy under identical conditions. As a first assessment, a stem is likely to be in the same motion regime (e.g. following Leclercq & De Langre 2018), when the wave period is the same, because $CaL/KC \propto (T_n\omega)^2$ is constant. On the one hand, the added mass increases from a single stem to multiple stems as known from offshore engineering for clusters of cylinders (Sarpkaya 1979; Heideman & Sarpkaya 1985) and it leads to an increase in T_n and thus CaL/KC. On the other hand, a large (nonlinear) mean deflection can change the natural period of the stem as seen for oscillating cantilever beams (Conzalez-Cruz, Jauregui-Correa & Herrera-Ruiz 2016). It is likely that buoyancy effects – otherwise neglected in this work – can have an influence on the natural period under large deflections. The nonlinear behaviour of the natural period, and thereby on the classification following CaL/KC, can be investigated with a validated nonlinear beam model.

The hydrodynamics within a canopy is influenced both by the intra-wave processes for vertical mixing and the period-averaged properties. The mean deflection of the stem, as discussed in § 3.3, is a clear proof that a mean force is acting on the stem, and there is thus an equal force acting on the water column. The mean force could potentially be important in a force equilibrium for the mean wave-induced set-up through and behind a canopy (Dean & Bender 2006; Wu *et al.* 2011), because the force equilibrium would otherwise only include terms from the bottom shear stress, the gradient in the mean surface elevation and the gradient in the radiation stress. Inclusion of a mean force on the vegetation in the horizontal force equilibrium (Van Rooijen *et al.* 2016; Zhu *et al.* 2019) thus balances part of the gradient in the radiation stress and reduces the equilibrium surface elevation gradient. The mean

force will also contribute to the shear stress distribution responsible for the mean flow within canopies (see e.g. Luhar *et al.* 2010; Abdolahpour *et al.* 2017, for experimental data on mean flow in canopies).

At present, the mean force is estimated based on streamfunction wave theory (Dean & Bender 2006), on the empirical wave shape by Ruessink, Ramaekers & Van Rijn (2012) as included in the XBeach model by Van Rooijen *et al.* (2016) or based on inclusion of second-order Stokes contributions in semi-analytical expressions of the mean force (Zhu *et al.* 2019). These approaches are reasonable for stiff stems; however, in the case of flexible stems, it is still not understood whether the nonlinear wave kinematics or the Lagrangian motion is governing $\bar{F}_x$. This should be quantified for a correct parameterization for large scale engineering models. The main contribution (Lagrangian motion or nonlinear kinematics) was investigated with the present experimental data, but the investigation was inconclusive. Therefore, it is recommended that a nonlinear numerical beam model be applied to resolve this outstanding question.

5. Conclusion

A unique data set for the motion of a single flexible stem with rectangular cross-section in regular waves was presented in this work. The data set distinguishes itself from previous laboratory studies by describing the full intra-wave motion of the stem and not only the displacement of the tip. A total of 48 combinations of stem properties (material properties and dimensions) and wave conditions were reported.

It was established that the non-dimensional quantity CaL/KC represents the motion characteristics better than the quantity CaL. This was linked to the similarity between CaL/KC and $(T_n\omega)^2$ (the latter by Leclercq & De Langre 2018). Leclercq & De Langre (2018) classified the response based on a ratio between the natural and wave periods. A small number of data points indicated that stems with a large mean deflection showed a different oscillatory behaviour from stems with a small mean deflection. This was explained by the fact that a large mean deflection restricts the oscillatory motion. This nonlinear effect cannot be described by existing theoretical models based on the linear Euler–Bernoulli beam theory and requires a nonlinear beam model such as those described in Dijkstra & Uittenbogaard (2010), Luhar & Nepf (2016) and Leclercq & De Langre (2018).

The phase lag between hydrodynamics and stem motion was evaluated and stiffer stems were seen to have a uniform phase lag over the length of the stem, while more flexible stems showed along-stem variation in the phase lag. This is linked to the importance of a second mode shape for more flexible stems.

The relative velocities and accelerations were evaluated and subsequently inserted into the dynamic beam model to calculate the average force coefficients for a flexible stem. Only the drag coefficient, C_D, was accurately extracted given the large value of KC, indicating a limited inertia force. It was seen that C_D showed better overall coherence as a function of the Keulegan–Carpenter number based on the relative velocities: the velocities which are effectively seen by the stem. The value of C_D decreases with increasing KC, which was attributed to linear drag for low KC and Re numbers.

The processing of the data allowed for approximations of both the external hydrodynamic loading and the internal shear force. It was seen that some stems had a monotonic increase of the shear force towards the base of the stem, while others exhibited a local maximum in the shear force closer to the top of the stem.

The local near-tip maximum was linked to the large variation of the phase lag over the length of the stem and thus also the motion regimes by Leclercq & De Langre (2018). The local maxima in the internal shear force (away from or at the base of the stem) can explain breakage mechanisms and thus loss of biomass.

The presented data set is envisaged as a valuable data set for benchmarking of linear and nonlinear numerical models for the motion of a single flexible stem in waves.

Acknowledgements

The authors would like to thank B. McFall (US Army Corps of Engineers), the three anonymous referees, and editor Professor J. T. Kirby for valuable comments. The lead author would furthermore thank Deltares' research programme 'Nature based Flood Defences' for financial support.

Supplementary movies

Supplementary movies are available at https://doi.org/10.1017/jfm.2019.739.

Appendix A. Matching measurements

There are several different signals that need to be synchronized to provide a reliable estimate of the force coefficients on the single stems. These signals are (i) synchronization of the velocity profile over the height of the water column, (ii) synchronization of the sampled velocity and force and (iii) synchronization of the video recording and the point measurements. These elements are described in the following sections.

A.1. *Reconstructing the velocity profile*

The two velocity components u and w were measured at a single location above the bed for each single test. Consequently, the velocity profile over the depth can only be reconstructed by a combination of several tests. The surface elevation, η, and velocity measurements both contained some low-frequency modulation, so an exact match of the time series was required to avoid temporal shifts in this modulation over the water column.

The synchronization of the velocity profile was based on the surface elevation at the same location as the mimic (WG5), see figure 1. The synchronization was done by evaluation of the correlation coefficient for η between two experiments, where one time series was given a temporal offset. The temporal offset leading to the largest correlation coefficient was adopted as the optimal synchronization. There were multiple velocity measurements for some vertical locations. In that case, the average velocity was used.

A.2. *Synchronization of force and velocity measurements*

There is an internal processing step in the EMF that leads to an offset between the sampling of the force transducer (no internal processing) and the EMF. The offset between the force transducer and the EMF was found to be approximately 0.11 s, i.e. 11 samples.

The offset was estimated by assuming that the maximum force for large velocities (large KC numbers) is drag dominated, i.e. correlated solely with $u|u|$ (Sumer &

Fredsøe 1999). A correlation analysis for 12 cases for the rigid mimic (mimic 4) with $KC > 100$ was performed and the force was found to lead the velocity signal by 0.08–0.14 s with an average of 0.114 s. The sampling frequency was 100 Hz, so an offset of 11 samples is used throughout this work. Hence, there is a synchronization error between force transducer and velocity of up to ± 0.03 s.

A.3. *Synchronization of footage and point measurements*

A LED was controlled by the acquisition system and the LED was captured by the digital video camera. The synchronization was automated by matching the control signal (point measurement) and the average of all pixel intensities in a frame (footage). The steering signal for the LED was set to activate the LED 1.12 s after the beginning of the control signal, so to avoid problems in the data treatment, the time signal for the LED was displaced manually by 1.12 s to a later time instance. The synchronization routine has a maximum uncertainty of 0.02 s, which equals half the time between each frame.

Appendix B. Outline of the stem tracking algorithm

The footage was acquired in colour (RGB), so the position of the stem could be identified on all three colour channels. This was used to actively decide on whether one of the colour channels resulted in an erroneous tracking. The criterion was that the position of the stem should be within 1 mm (2.5 pixels) of each other on the three colour channels to qualify as a valid tracking. If not, the position of the stem was regarded as unknown (see e.g. figure 17*b*).

The basis of the stem tracking is as follows:

(i) Load all footage (except for frames with the LED on) into the matrices $\boldsymbol{X}_0$, $\boldsymbol{X}_1, \ldots, \boldsymbol{X}_N$ of rank 3 (the third dimension contains each of the three colour channels).

(ii) Evaluate the simple mean of the pixel intensity of these frames ($\overline{\boldsymbol{X}}$) and compute the perturbation from this mean $\boldsymbol{X}'_n = \boldsymbol{X}_n - \overline{\boldsymbol{X}}$. This step effectively removed the EMF from the footage (which is otherwise present, see figure 17).

(iii) Perform a Gaussian blur of the frames, where the size of the blurring kernel is 7-by-7 pixels. This step is used to reduce noise away from the stem, which would otherwise (erroneously) be considered part of the stem.

(iv) Perform edge detection with a compact kernel. (The compact kernel reads $\boldsymbol{K} = [-2, 0, 2; -1, 0, 1; -2, 0, 2]$ for detection along one axis and $\boldsymbol{K}^T$ for detection along the second axis.) The edge detection allows for evaluation of sharp gradients in $\boldsymbol{X}'$.

(v) Large values of the gradient in pixel intensity are tracked from the root of the stem and upward. The tracking for each frame is stopped, when either the tracked length of the stem equals the full length of the stem (figure 17*f*) or the position of the stem is too blurred to provide a reliable tracking (figure 17*b*).

The position of the root of the stem was identified manually prior to the execution of the automated tracking procedure. Examples of the raw footage and the result of the tracking algorithm are shown in figure 17.

It was not always possible to detect the end of the stem with the tracking algorithm, since the velocity of the stem occasionally exceeded 0.3–0.4 m s^{-1} (figure 17*b*), which meant that the stem displaced more than 30 pixels within one frame. High

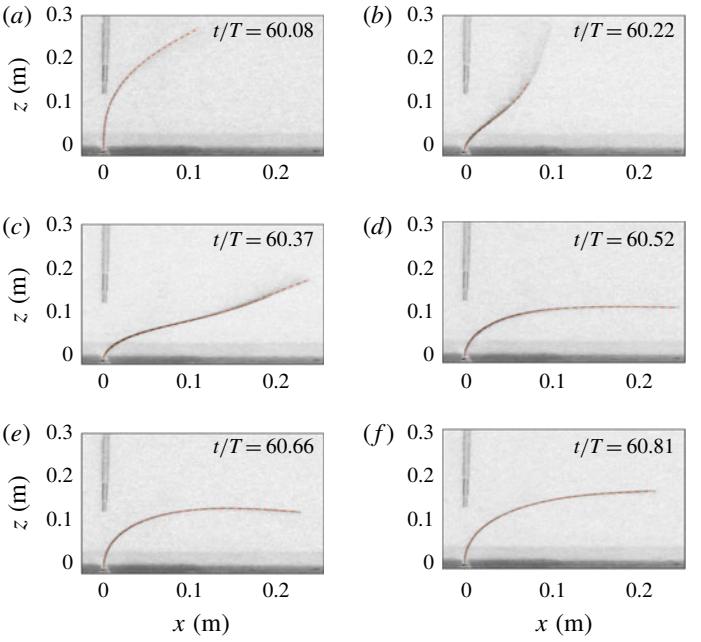

FIGURE 17. (Colour online) Example of the tracking algorithm for six frames for a case with mimic 2 and $l = 0.30$ m. The vertical lines at $x = 0$ m are the EMF. The dashed orange line is the tracked position of the stem. Panel (*b*) shows an example where a part of the stem was not recognized.

speed cameras, optimal lighting and a short shutter time are all recommended for future works.

The blurring of the stem during the sweeping from one extreme position to another means that the location during this part of the motion is not always captured. However, the velocity of the stem vanishes in the extreme positions, which is why a reliable tracking of the extremities of the stem location was achieved for all tests with mimic 2 and 3.

The tracked position of the stem $(x_s(s), z_s(s))$ was finally interpolated onto an equidistant coordinate system along the length of the stem, s. The resolution was set to $\Delta s = 2.5$ mm, which is approximately 6 pixels.

Appendix C. Deriving the stem velocity and acceleration

At first, it was attempted to evaluate the velocities $(\partial x_s/\partial t)$ and accelerations $(\partial^2 x_s/\partial t^2)$ of the stem segments with a simple 3-point finite difference stencil. This resulted in an accumulation of noise for each additional derivative (figure 18). The noise was expected to affect the fitting to the Morison equation, when deriving the force coefficients, why a different method was adopted.

Proper orthogonal decomposition was applied on the coordinate sets (x_s, z_s). This method allows for the evaluation of case specific mode shapes $\boldsymbol{\Phi}_s$ and the associated weights $\alpha_s(t)$. The POD method is not detailed in this work, so reference is made to e.g. Birkemeier (1984) and Jacobsen, van Velzen & Fredsøe (2014). Examples of mode shapes are shown in figures 4 and 19, and merely two mode shapes are enough to characterize 98.5 % of the motion for that particular example.

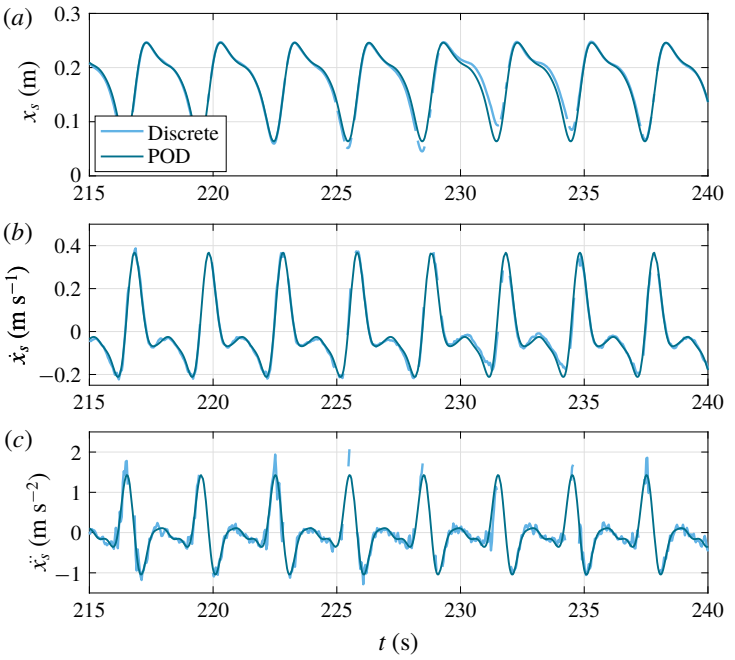

FIGURE 18. (Colour online) Example of x_s, $\dot{x}_s$ and $\ddot{x}_s$ at the tip of the stem for $l = 0.30$, $T = 3.0$ s and $H = 0.11$ m (Mimic 2). The finite difference (discrete) and POD approach to evaluate $\dot{x}_s$ and $\ddot{x}_s$ are shown.

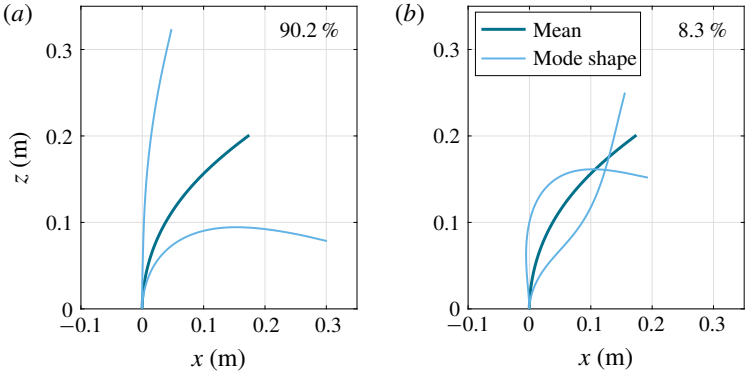

FIGURE 19. (Colour online) The two first mode shapes and the mean stem position. Same stem as in figure 18. The percentage is the importance of the mode in the description of the fluctuating motion.

The strength of the POD method is that the stem position can be reconstructed as follows:

$$[\boldsymbol{x}_s; \boldsymbol{z}_s] = [\overline{\boldsymbol{x}}_s; \overline{\boldsymbol{z}}_s] + \sum_n \alpha_{s,n}(t)\boldsymbol{\Phi}_{s,n}, \tag{C 1}$$

where bold symbols are column vectors and n is the nth mode shape. Consequently, the stem velocities and accelerations read

$$[\dot{\boldsymbol{x}}_s;\dot{\boldsymbol{z}}_s]=\sum_n \dot{\alpha}_{s,n}\boldsymbol{\Phi}_{s,n} \quad \text{and} \quad [\ddot{\boldsymbol{x}}_s;\ddot{\boldsymbol{z}}_s]=\sum_n \ddot{\alpha}_{s,n}\boldsymbol{\Phi}_{s,n}. \tag{C 2a,b}$$

Evaluation of $\dot{\alpha}_s$ and $\ddot{\alpha}_s$ with a finite difference scheme would introduce noise as well. Consequently, α_s was first estimated with the following fit (filter):

$$\tilde{\alpha}_s = a_0 + \sum_{n=1}^{5} a_n \cos n\omega t + b_n \sin n\omega t, \tag{C 3}$$

where $\omega = 2\pi/T$ is the cyclic frequency and the fit is limited to the first five harmonics. This fitting is possible because regular waves were used. The temporal derivatives are then estimated through algebraic differentiation instead of a numerical equivalent

$$\dot{\tilde{\alpha}}_s = \sum_{n=1}^{5} n\omega(-a_n \sin n\omega t + b_n \cos n\omega t) \tag{C 4}$$

and

$$\ddot{\tilde{\alpha}}_s = \sum_{n=1}^{5} n^2\omega^2(-a_n \cos n\omega t - b_n \sin n\omega t). \tag{C 5}$$

The fitting approach in (C 3) was favoured over a Fourier decomposition of α_s for two reasons: (i) The time series for α_s are non-equidistant, which makes discrete Fourier transforms less straightforward. (ii) The match to the exact frequency ω instead of a discrete frequency originating from a discrete Fourier transform was expected to result in more accurate approximations of $\dot{\tilde{\alpha}}_s$ and $\ddot{\tilde{\alpha}}_s$.

The associated velocity and acceleration are shown in figure 18 and a noise reduction is seen. The drawback of the adopted approach is that slow variations in the stem motion are not included, so the POD-method results in a regularization of the signal. This will not have any consequence for the present analysis of the force coefficients, because the slow motion only affects the velocities and accelerations with small modifications, which are estimated to be $O(1\,\%)$.

Appendix D. Supplementary video material

Four videos are added as supplementary material. The videos have four panels showing (i) stem and relative velocities, (ii) the distributed, horizontal forces on the stem, (iii) the stem and relative accelerations and (iv) the distributed shear force in the stem. Metadata is provided in the footer of the video.

The four videos match the example cases used throughout this paper (e.g. figures 3 and 4). Movie 1 corresponds to figure 3(*a*), Movie 2 corresponds to figure 3(*b*), etc.

REFERENCES

ABDOLAHPOUR, M., HAMBLETON, M. & GHISALBERTI, M. 2017 The wave-driven current in coastal canopies. *J. Geophys. Res.: Oceans* **122**, 1–15.

ANDERSON, M. E. & SMITH, J. M. 2014 Wave attenuation by flexible, idealized salt marsh vegetation. *Coast. Engng* **83**, 82–92.

BIRKEMEIER, W. A. 1984 Time scales of nearshore profile changes. *Proc. Coast. Engng Conf.* **II**, 1507–1521.

BRADLEY, K. & HOUSER, C. 2009 Relative velocity of seagrass blades: implications for wave attenuation in low-eenrgy environments. *J. Geophys. Res.* **114**, 1–13.

CHEN, H. & ZOU, Q.-P. 2019 Eulerian-Lagrangian flow-vegetation interaction model using immersed boundary method and OpenFOAM. *Adv. Water Resour.* **126**, 176–192.

CONZALEZ-CRUZ, C. A., JAUREGUI-CORREA, J. C. & HERRERA-RUIZ, G. 2016 Nonlinear response of cantilever beams due to large geometric deformations: experimental validation. *J. Mech. Engng* **62** (3), 187–196.

DEAN, R. G. & BENDER, C. J. 2006 Static wave setup with emphasis on damping effects by vegetation and bottom friction. *Coast. Engng* **53**, 149–156.

DEIGAARD, R. & FREDSØE, J. 1989 Shear-stress distribution in dissipative water-waves. *Coast. Engng* **13** (4), 357–378.

DEIGAARD, R., JUSTESEN, P. & FREDSØE, J. 1991 Modeling of undertow by a one-equation turbulence model. *Coast. Engng* **15** (5–6), 431–458.

DIJKSTRA, J. T. & UITTENBOGAARD, R. E. 2010 Modeling the interaction between flow and highly flexible aquatic vegetation. *Water Resour. Res.* **46**, W12547, 14 pages.

DUBI, A. & TØRUM, A. 1994 Wave damping by kelp vegetation. *Proc. Coast. Engng Conf.* **I**, 142–156.

EurOtop 2018 Manual on wave overtopping of sea defences and related structures. An overtopping manual largely based on European research, but for worldwide application. Van der Meer, J. W., Allsop, N. W. H., Bruce, T., De Rouck, J., Kortenhaus, A., Pullen, T., Schüttrumpf, H., Troch, P. and Zanuttigh, B. Available at: www.overtopping-manual.com.

FOSTER-MARTINEZ, M. R., LACY, J. R., FERNER, M. C. & VARIANO, E. A. 2018 Wave attenuation across a tidal march in San Francisco Bay. *Coast. Engng* **138**, 26–40.

GIJÓN MANCHEÑO, A. 2016 Interaction between wave hydrodynamics and flexible vegetation. Master's thesis, Delft University of Technology.

GUANNEL, G. & ÖZKAN-HALLER, H. T. 2014 Formulation of the undertow using linear wave theory. *Phys. Fluids* **26**, 1–18.

HEIDEMAN, J. C. & SARPKAYA, T. 1985 Hydrodynamic forces on dense arrays of cylinders. In *Offshore Technology Conference*, pp. 421–428. Offshore Technology Conference.

JACOBSEN, N. G., MCFALL, B. C. & VAN DER A, D. A. 2019 A frequency distributed dissipation model for canopies. *Coast. Engng* **150**, 135–146.

JACOBSEN, N. G., VAN VELZEN, G. & FREDSØE, J. 2014 Analysis of pile scour and associated hydrodynamic forces using proper orthogonal decomposition. In *Scour and Erosion: Proceedings of the 7th International Conference on Scour and Erosion, Perth, Australia, 2–4 December 2014*, p. 361. CRC Press.

JADHAV, R. S., CHEN, Q. & SMITH, J. M. 2013 Spectral distribution of wave energy dissipation by salt marsh vegetation. *Coast. Engng* **77**, 99–107.

LECLERCQ, T. & DE LANGRE, E. 2018 Reconfiguration of elastic blades in oscillatory flow. *J. Fluid Mech.* **838**, 606–630.

LEI, J. & NEPF, H. 2019 Wave damping by flexible vegetation: connecting individual blade dynamics to the meadow scale. *Coast. Engng* **147**, 138–148.

LOSADA, I. J., MAZA, M. & LARA, J. L. 2016 A new formulation for vegetation-induced damping under combined waves and currents. *Coast. Engng* **107**, 1–13.

LUHAR, M., COUTU, S., INFANTES, E., FOX, S. & NEPF, H. 2010 Wave-induced velocities inside a model seagrass bed. *J. Geophys. Res.* **115** (C12005), 1–15.

LUHAR, M. & NEPF, H. 2011 Flow-induced reconfiguration of buoyant and flexible aquatic vegetation. *Limnol. Oceanogr.* **56** (6), 2003–2017.

LUHAR, M. & NEPF, H. M. 2016 Wave-induced dynamics of flexible blades. *J. Fluids Struct.* **61**, 20–41.

MAZA, M., LARA, J. L. & LOSADA, I. J. 2013 A coupled model of submerged vegetation under oscillatory flow using Navier–Stokes equations. *Coast. Engng* **80**, 16–34.

MAZA, M., LARA, J. L., LOSADA, I. J., ONDIVIELA, B., TRINOGGA, J. & BOUMA, T. J. 2015 Large-scale 3-D experiments of wave and current interaction with real vegetation. Part 2: experimental analysis. *Coast. Engng* **106**, 73–86.

MÖLLER, I, KUDELLA, M., RUPPRECHT, F., SPENCER, T., PAUL, M., VAN WESENBEECK, B. K., WOLTERS, G., JENSEN, K., BOUMA, T. J., MIRANDA-LANGE, M. & SCHIMMELS, S. 2014 Wave attenuation over coastal salt marches under storm surge conditions. *Nature Geosci.* **7**, 727–731.

MULLARNEY, J. C. & HENDERSON, S. M. 2010 Wave-forced motion of submerged single-stem vegetation. *J. Geophys. Res.* **115**, C12061.

MULLARNEY, J. C. & PILDITCH, C. A. 2017 The differential response of kelp to swell and infragravity wave motion. *Limnol. Oceanogr.* **62** (6), 2524–2537.

PUJOL, D., SERRA, T., COLOMER, J. & CASAMITJANA, X. 2013 Flow structure in canopy models dominated by progressive waves. *J. Hydrol.* **486**, 281–292.

ROS, A., COLOMER, J., SERRA, T., PUJOL, D., SOLER, M. & CASAMITJANA, X. 2014 Experimental observations on sediment resuspension within submerged model canopies under oscillatory flow. *Cont. Shelf Res.* **91**, 220–231.

RUESSINK, B. G., RAMAEKERS, G. & VAN RIJN, L. C. 2012 On the parameterization of the free-stream non-linear wave orbital motion in nearshore morphodynamic models. *Coast. Engng* **65**, 56–63.

SARPKAYA, T. 1979 Hydrodynamic forces on various multiple-tube riser configurations. *Offshore Technol. Conf.* 1603–1606.

SUMER, B. M. & FREDSØE, J. 1999 *Hydrodynamics around Cylindrical Structures*, 1st edn. Advanced Series on Coastal Engineering, vol. 12. World Scientific.

SUZUKI, T., ZIJLEMA, M., BURGER, B., MEIJER, M. C. & NARAYAN, S. 2012 Wave dissipation by vegetation with layer schematization in SWAN. *Coast. Engng* **59**, 64–71.

TINOCO, R. O. & COCO, G. 2018 Turbulence as the main driver of resuspension in oscillatory flow through vegetation. *J. Geophys. Res. Earth Surf.* **123**, 1–14.

VAN ROOIJEN, A. A., MCCALL, R. T., VAN THIEL DE VRIES, J. S. M., VAN DONGEREN, A. R., RENIERS, A. J. H. M. & ROELVINK, J. A. 2016 Modeling the effect of wave-vegetation interaction on wave setup. *J. Geophys. Res. Oceans* **121**, 1–19.

VO-LUONG, P. & MASSEL, S. 2008 Energy dissipation in non-uniform mangrove forests of arbitrary depth. *J. Mar. Syst.* **74** (1), 603–622.

VUIK, V., VAN VUREN, S., BORSJE, B. W., VAN WESENBEECK, B. K. & JONKMANN, S. N. 2018 Assessing satefy of nature-based flood defenses: Dealing with extremes and uncertainties. *Coast. Engng* **139**, 47–64.

WU, W., OZEREN, Y., CHEN, Q., HOLLAND, M., DING, Y., KUIRY, S. N., ZHANG, M., JADHAV, R., CHATAGNIER, J., CHEN, Y. & GORDJI, L. 2011 Phase I report for SERRI project no. 80037: investigation of surge and wave reduction by vegetation. *Tech. Rep.* 80037-01. National Center for Computational Hydroscience and Engineering; The University of Mississippi.

ZELLER, R. B., WEITZMAN, J. S., ABBETT, M. E., ZARAMA, F. J., FRINGER, O. B. & KOSEFF, J. R. 2014 Improved parameterization of seagrass blade dynamics and wave attenuation based on numerical and laboratory experiments. *Limnol. Oceanogr.* **59** (1), 251–266.

ZHANG, Y. & NEPF, H. 2019 Wave-driven sediment resuspension within a model eelgrass meadow. *J. Geophys. Res. Earth Surf.* **124**, 1–19.

ZHU, L., CHEN, Q., DING, Y., JAFARI, N. & ROSATI, J. D. 2019 Semianalytical model of depth-integrated vegetal drag force based on Stokes second-order wave theory. *ASCE J. Waterway Port Coastal Ocean Engng* **145** (2), 1–13.